

The circumbinary disk of HD 34700A

I. CO gas kinematics indicate spirals, infall, and vortex motions

J. Stadler^{1,2}, M. Benisty³, F. Zagaria³, A. F. Izquierdo^{4,5}, J. Speedie^{6,7,8}, A. J. Winter^{9,3}, L. Wölfer⁷, J. Bae⁴, S. Facchini¹⁰, D. Fasano^{1,3}, N. Kurtovic¹¹, R. Teague⁷

¹ Université Côte d'Azur, Observatoire de la Côte d'Azur, CNRS, Laboratoire Lagrange, France

² European Southern Observatory, Karl-Schwarzschild-Str. 2, 85748 Garching bei München, Germany

e-mail: jochen.stadler@eso.org

³ Max-Planck Institute for Astronomy (MPIA), Königstuhl 17, 69117 Heidelberg, Germany

⁴ Department of Astronomy, University of Florida, Gainesville, FL 32611, USA

⁵ NASA Hubble Fellowship Program Sagan Fellow

⁶ Department of Physics & Astronomy, University of Victoria, Victoria, BC, V8P 5C2, Canada

⁷ Department of Earth, Atmospheric, and Planetary Sciences, Massachusetts Institute of Technology, Cambridge, MA 02139, USA

⁸ Heising-Simons Foundation 51 Pegasi b Fellow

⁹ Astronomy Unit, School of Physics and Astronomy, Queen Mary University of London, London E1 4NS, UK

¹⁰ Università degli Studi di Milano, via Celoria 16, 20133 Milano, Italy

¹¹ Max Planck Institute for Extraterrestrial Physics, Giessenbachstrasse 1, D-85748 Garching, Germany

Submitted on July 29 2025; accepted for publication in A&A on January 16, 2026.

ABSTRACT

Aims. We present the first high-resolution ($\sim 0''.14$) Atacama Large Millimeter/submillimeter Array (ALMA) Band 6 dust continuum, ^{12}CO $J = 2 - 1$, ^{13}CO $J = 2 - 1$, and C^{18}O $J = 2 - 1$ molecular line emission observations of the quadruple system HD 34700. In particular, HD 34700AaAb is a spectroscopic binary ($M_{\text{bin}} = 4 M_{\odot}$) surrounded by two low-mass companions (B= $0.6 M_{\odot}$, C= $0.4 M_{\odot}$) at large separations. Its circumbinary disk is highly substructured, featuring numerous spiral arms and a large cavity observed in infrared (IR) scattered light. We aim to shed light on the nature of these features by examining the gas kinematics at work in the circumbinary disk.

Methods. We analyzed the CO line channel and intensity moment maps. By fitting a Keplerian model to the line channel emission, we identified the residual motions and conducted a line spectra analysis.

Results. We resolved an asymmetric continuum crescent on top of a dust ring at $0''.39$ (138 au) colocated with the IR ring. The CO molecule's line emission traces a smaller cavity in gas, whose edge aligns with the inner rim of the ring detected in $\text{H}\alpha$ emission at $0''.20$ (65 au). The ^{12}CO line emission and kinematics trace highly non-Keplerian motions ($\sim 0.1\Delta v_k$) and these CO spiral features align well with the spiral structures in scattered light. The ^{12}CO line spectra analysis reveals a streamer above the southeastern disk plane, likely falling onto the disk. The ^{13}CO and C^{18}O kinematics largely follow the disk's underlying Keplerian rotation, while ^{13}CO exhibits tentative signs of anticyclonic vortex flows at the continuum crescent location.

Conclusions. Our multimolecular line study suggests that the circumbinary disk of HD 34700A is highly perturbed in its upper layers, possibly warped and influenced by infalling material. While late-stage infall may account for the IR spirals and the formation of the vortex through Rossby wave instability, an embedded massive companion within the cavity might also be contributing to these features.

Key words. planets and satellites: formation – protoplanetary disks – planet-disk interactions – ISM: individual objects (HD 34700)

1. Introduction

A high fraction of stars are born in multiple systems (Offner et al. 2023). The presence of stellar companions can significantly influence the evolution of protoplanetary disks. Tidal interactions can affect the morphology of protoplanetary disks through the formation of spirals, misalignment, and truncation (see Cuello et al. 2025, for a recent review). Consequently, these gravitational interactions are crucial in determining the disks' potential for planetary formation (Marzari & Thebault 2019). Planets have been observed in multiple systems, with over 700 planets detected around single stars (S-type) and over 30 or-

biting a binary star (P-type, Thebault & Bonanni 2025). In circumbinary disks (CBDs), the tidal forces created by the binary system carve out a cavity in the inner region of the disk, whose size is roughly a few times the separation of the binary (Artymowicz & Lubow 1994; Hirsh et al. 2020; Penzlin et al. 2024). In the case of a high mass ratio in binary systems ($q = M_2/M_1 > 0.05$), the cavity becomes eccentric and develops horseshoe-shaped structures (e.g., Ragusa et al. 2020). Identifying such substructures in gas and dust observations can provide clues about the presence of massive companions (e.g., Ragusa et al. 2021; Kurtovic et al. 2022; Calcino et al. 2023, 2024).

In this work, we focus on the ~ 5 Myr old (Monnier et al. 2019) quadruple system HD 34700 (HIP 24855; $d=350.9 \pm 2.4$ pc; Gaia Collaboration et al. 2023). It consists of a close ($a_{\text{bin}}=0.69$ au) near-equal-mass Herbig Ae spectroscopic binary ($M_{\text{bin}} = 4M_{\odot}$, HD 34700 AaAb; hereafter, HD 34700A) and two low-mass M-type companions located at distances of $5''.2$ (B, $\sim 0.6M_{\odot}$) and $9''.3$ (C, $\sim 0.4M_{\odot}$; Sterzik et al. 2005). The system was first observed by Monnier et al. (2019) in near-infrared (NIR) scattered light with Gemini/GPI. They found that the binary is surrounded by a disk with a cavity and multiple substructures. As shown in Fig. 1a, it displays a large inner dust-depleted cavity surrounded by a wide elliptic ring-like feature at $R = 175$ au, from which at least six spirals with extensive opening angles ($\sim 30^{\circ}$ to 50°) originate. Interestingly, these observations revealed a discontinuity toward the north of the ring, which was later confirmed by Subaru/SCExAO and SPHERE observations (Uyama et al. 2020; Columba et al. 2024), together with several shadows on the ring and spirals, suggesting the presence of an inclined inner disk or a warp. Recent observations further detected a symmetric ring in H α emission ($R = 65$ – 120 au) inside the asymmetric IR ring (Fig. 1b), tracing sub- μm -sized dust particles (Columba et al. 2024). Low-resolution ($\lesssim 0''.35$) Submillimetre Array (SMA) and ALMA observations revealed a prominent azimuthal asymmetry in the mm continuum, located at the edge of the scattered-light cavity (Benac et al. 2020; Columba et al. 2024).

Continuum asymmetries can arise from azimuthally trapped dust particles (Birnstiel et al. 2013; Bae et al. 2016). This trapping occurs in local pressure maxima, which could develop due to anticyclonic vortices caused by the Rossby wave instability (RWI, Lovelace et al. 1999; Li et al. 2000). For the RWI to be triggered, the disk must show strong gas density gradients, which tend to be present at the edges of gas cavities (e.g., Bracco et al. 1999). Other favorable mechanisms include dead zones (Flock et al. 2015, 2017) or the anisotropic infall of material (Bae et al. 2015; Kuznetsova et al. 2022). To sustain the RWI and observe long-lived anticyclonic vortices, the turbulence within the disk must remain low ($\alpha \lesssim 10^{-3}$, Li et al. 2000). Besides local over-densities in dust rings, pronounced dust continuum crescents have only been observed in a few transition disks, such as IRS 48 (van der Marel et al. 2013) and HD 142527 (Casassus et al. 2013). Although several attempts have been made to characterize gas motions around these crescents and to determine whether they can be explained by vortices (Robert et al. 2020; Boehler et al. 2021; van der Marel et al. 2021; Wölfer et al. 2025), the results have thus far remained inconclusive due to the complexity of the disk kinematics and the limited resolution of these observations.

The multiple IR spirals in HD 34700A and their varying opening angles remain challenging to explain. Gravitational instability and stellar flybys have been considered unlikely (Monnier et al. 2019; Shuai et al. 2022, respectively). Additionally, the binary separation is too small (< 1 au) to allow for any periodic perturbation over its orbit, which would be needed to drive the spirals. A possible explanation for the origin of the observed features is the presence of a massive companion of a few Jupiter masses located within the cavity, along with the system's interaction with its surrounding environment (Monnier et al. 2019; Columba et al. 2024). Recent disk observations have reported some of the effects of late-stage infall of ambient material from the molecular cloud (e.g., Garufi et al. 2024; Gupta et al. 2023; Huang et al. 2020, 2021, 2023; Speedie et al. 2025) in disks that show extended spiral features. Theoretical studies show that these processes can initiate and sustain spiral arms for

several thousand years after the infall event (Dong et al. 2016; Calcino et al. 2025a; Kuffmeier et al. 2020) and can also lead to disk warping (e.g., Akeson et al. 2007; Dullemond et al. 2019; Kuffmeier et al. 2021; Young et al. 2022).

This paper presents new ALMA Band 6 continuum and CO molecular line observations at high-resolution toward HD 34700 and is structured as follows. In Sect. 2 we describe the observations, applied calibration, and imaging choices. Section 3 explains the methodology used to fit the CO kinematic data. Our results are presented in Sect. 4, with subsections on the continuum crescent, molecular line emission and kinematics, and line spectra analysis. Finally, we discuss our findings in Sect. 5 and state our conclusions in Sect. 6.

2. Observations, calibration, and imaging

We present new ALMA Band 6 observations of the quadruple system HD 34700 (2022.1.00760.S; PI: Stadler) with two short-baseline (SB) and eleven long-baseline (LB) execution blocks (EBs), with total on-source time of 1.6 h and 8.6 h, respectively. The SB observations in configuration C-3 were taken on October 9, 2022 with a mean precipitable water vapor (PWV) of 0.3 mm. The LB executions in C-6 spanned three weeks with a mean PWV in the range of 0.3 to 1.4 mm. Details on the EB measurement sets are listed in Table A.1. The spectral setup was designed to study the kinematics of the circumbinary disk. Thus, one spectral window (SPW) was centered on the $^{12}\text{CO } J = 2 - 1$ line at a native spectral resolution of 92 m s^{-1} (70.6 kHz) and one around the $^{13}\text{CO } J = 2 - 1$ and $\text{C}^{18}\text{O } J = 2 - 1$ molecular lines, both at 192 m s^{-1} (141 kHz). The remaining two SPWs target the continuum emission centered at 218.0 and 232.6 GHz, each with a bandwidth of 1.9 GHz and native frequency spacing of 1.13 MHz ($\sim 1.5\text{ km s}^{-1}$ native channel spacing).

The data calibration and imaging were performed using CASA v. 6.2.1 (CASA Team et al. 2022) following the procedure of the exoALMA collaboration presented in Loomis et al. (2025). This pipeline was designed explicitly for high angular and spectral resolution kinematical data. Starting with the pipeline-calibrated data, we applied self-calibration (self-cal) to all of our EBs. First, we flagged any prominent line emission detected in each SPW and then spectrally averaged the EBs by a factor of 12. This pre-averaging did not show any significant negative effect on the final obtained images as shown in Curone et al. (2025). Following the exoALMA pipeline, we performed one phase-only self-calibration round with solution intervals of `solint='inf'` on each EB, before spatially aligning and concatenating the individual SB and LB EBs. We then conducted three rounds of phase-only self-cal (`solint=['inf', 340s, 120s]`) on the concatenated SB observations and combined them with the LB EBs. Three additional rounds of phase self-cal (`solint=['inf', 340s, 120s]`) and one round of amplitude and phase self-cal (`solint='inf'`) were performed on the concatenated dataset, increasing the final continuum signal-to-noise ratio (S/N) by over 30% compared to the concatenated non-calibrated dataset. These self-calibration tables were then applied to the whole data set, including the molecular lines. Finally, a continuum subtraction was performed before splitting out the final line emission measurement set (ms) tables.

The continuum was imaged using two manually adapted ellipses: one centered on HD 34700A with a semi-major axis of $1''.2$ and an inclination of 40° and a second centered on HD 34700B with a radius of $0''.5$ and an inclination of 26° . For the molecular line imaging, we followed the procedure outlined in Loomis et al. (2025, see their Fig. 10).

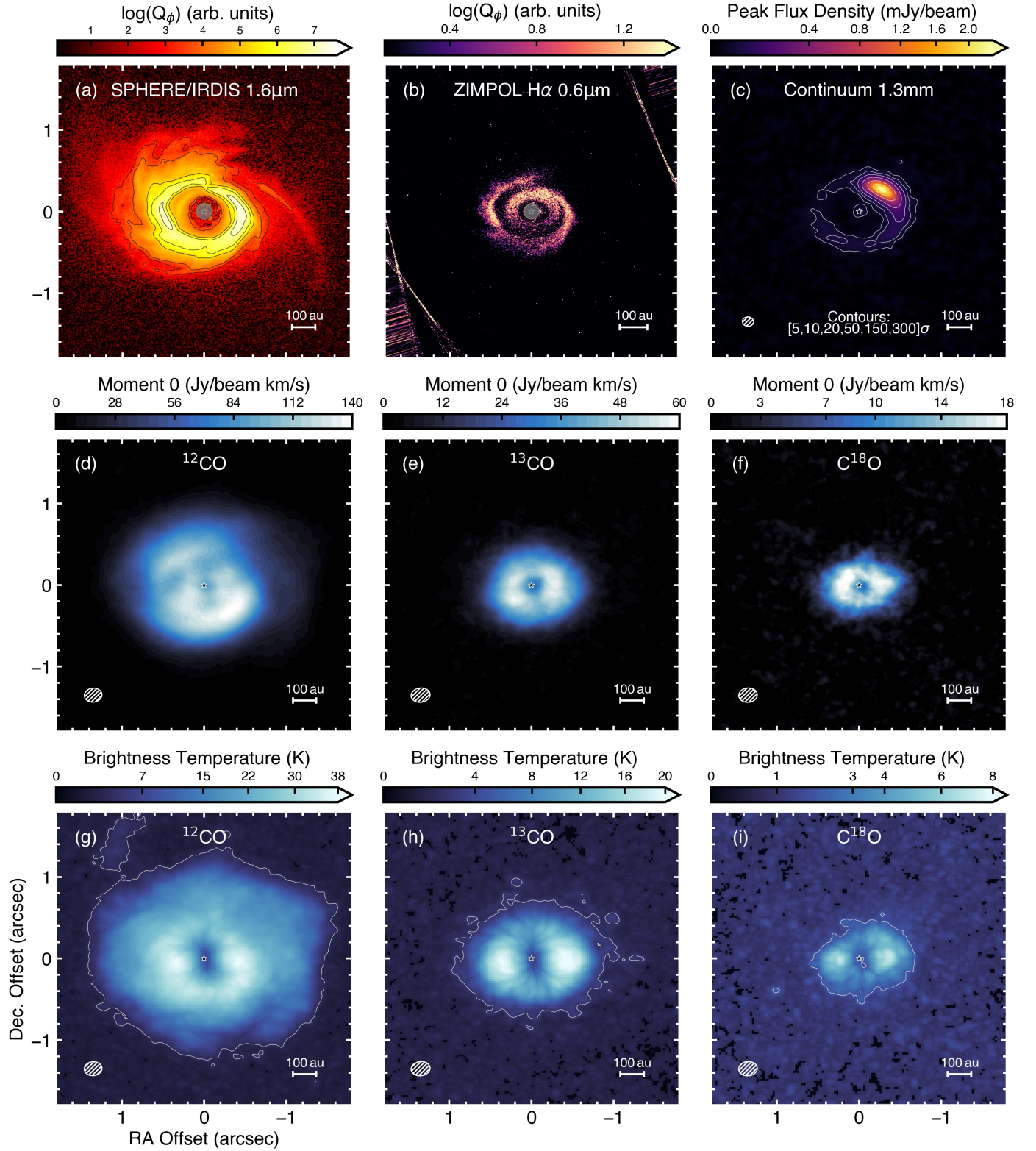


Fig. 1: Multi-wavelengths observations of HD 34700A. (a) SPHERE/IRDIS IR scattered light observations and (b) ZIMPOL H α observations presented in Columba et al. (2024), with the gray circles representing the coronograph ($r = 92.5$ mas ≈ 32 au). (c) ALMA 225.3 GHz continuum observations. (d), (e), and (f) show the moment 0 maps for the ^{12}CO , ^{13}CO , and C^{18}O fiducial cubes, while (g), (h), and (i) show the peak intensity maps for the same cubes, respectively. The brightness temperature was computed using the Rayleigh-Jeans approximation. The white contour in the peak intensity maps encloses 5σ of the root-mean-square (RMS) noise of each line. The location of the spectroscopic binary is highlighted with the star. The beam size is shown in the lower left corner for the ALMA observations.

The continuum images presented in this paper were imaged CLEANing down to 3 sigma and with robust parameters (rob.) of 0.5 and -1.5 (Briggs 1995), corresponding to synthesized beams of 137×115 mas 2 (86.3°) and 92×66 mas 2 (87.3°), respectively.

The resulting RMS noise levels are $5.1 \mu\text{Jy beam}^{-1}$ (rob. 0.5) and $22.7 \mu\text{Jy beam}^{-1}$ (rob. -1.5). We measured the peak continuum intensity for the robust 0.5 image to be $2.32 \text{ mJy beam}^{-1}$ ($\text{S/N} = 458\sigma$) with a total flux density of $8.42 \pm 0.8 \text{ mJy}$ (10% absolute flux error in ALMA Band 6) within the CLEAN mask, in line with previous measurements (Benac et al. 2020; Columba et al. 2024).

The CO molecular lines were CLEANed down to a threshold of 3σ and then imaged using a robust parameter of 1.5 to obtain the “fiducial” high-sensitivity images and a robust parameter of 0.5 to obtain “high-resolution” images. These robust values result in synthesized beams of $0''.22 \times 0''.17$ (96.0°) and $0''.14 \times 0''.11$ (88.8°). For the $^{12}\text{CO } J = 2 - 1$ image cubes, we measured an RMS noise outside the CLEAN mask of $0.99 \text{ mJy beam}^{-1}$ (rob. 1.5, RMS noise in the Rayleigh-Jeans approximation: 0.62 K) and $1.12 \text{ mJy beam}^{-1}$ (rob. 0.5, 1.65 K) both with 100 m s^{-1} channels. The $^{13}\text{CO } J = 2 - 1$ and $\text{C}^{18}\text{O } J = 2 - 1$ emission lines were imaged with 200 m s^{-1} channels and have noise levels of $[0.74, 0.85] \text{ mJy beam}^{-1}$ ($[0.46, 1.2] \text{ K}$) and $[0.59, 0.68] \text{ mJy beam}^{-1}$ ($[0.38, 1.0] \text{ K}$) on the robust $[1.5, 0.5]$ cubes, respectively. An overview of the above-mentioned imaging parameters, RMS noises, and flux densities, for the continuum and CO molecular lines can be found in Table A.2.

In the following, we solely focus on analyzing the circumbinary disk HD 34700A. The observations and analysis of the circumstellar disk around binary companion HD 34700B are presented in Appendix B. We note that we did not detect any significant ($> 3\sigma$) continuum or molecular line emission at the positions of either HD 34700C or proposed companion D ($6''.45$ along $\text{PA} \approx -61^\circ$ Monnier et al. 2019), nor any emission that bridges over HD 34700A and B.

3. Methodology

We employed the `discminer` code package (Izquierdo et al. 2021) to model the molecular line emission channel-by-channel and analyze the disk gas kinematics. This state-of-the-art code fits a Keplerian model to the local line profile of each spatial pixel i and velocity channel, j , that maximizes the log-likelihood function

$$\log \mathcal{L} = -0.5 \sum_j \sum_i \left[I_m(r_i, v_j) - I_d(r_i, v_j) \right]^2 / \sigma_i^2, \quad (1)$$

between the observed I_d and model intensity I_m . Each pixel is weighted by a factor, σ_i , with the standard deviation of its intensity measured in line-free channels, analogously to the RMS noise. To obtain the best-fit model parameters, the code utilizes Markov chain Monte Carlo (MCMC) ensemble sampler `emcee` (Foreman-Mackey et al. 2019) to sample the parameter posterior distribution. The model is parametrized in the radial direction using a double-power law for the peak intensity and a monotonically decreasing one for the linewidth. The disk surface height is described by an exponentially tapered power law, which is assumed to be infinitely narrow, and the velocity is a Keplerian profile corrected for the surface heights $v_K(R, z)$ (see Izquierdo et al. 2025, for functional forms).

We fit each molecular line tracer independently, employing the high-resolution cubes for ^{12}CO and ^{13}CO and fiducial cube for C^{18}O . For the initial parameter guesses in each run, we adopted the literature values for combined stellar mass of the spectroscopic binary ($M_\star = 4.0 M_\odot$) and inclination ($i_0 = 40^\circ$; Torres 2004; Columba et al. 2024). For the remaining parameters, including position angle PA, systemic velocity

v_{LSRK} , and power-law profiles for the intensity, line-width, and line-slope, we estimated the starting values using a preliminary `discminer` model prototype applied to the data channels. We did not prescribe a back surface in the model, as the channel maps and line profiles did not show any contribution from it (see Izquierdo et al. 2025, for a detailed discussion). In other words, we only observe the disk’s near-side. For a disk seen at a moderate inclination of $i = 40^\circ$, this hints toward a relatively flat disk emission height. Furthermore, we masked the innermost beam size in diameter from the disk center due to cavity and beam smearing effects. We employed 200 walkers for 21 parameters and ran the fits for 37,000 (^{12}CO), 20,000 (^{13}CO), and 15,000 (C^{18}O) steps until the marginalized posteriors were reasonably well converged and Gaussian. The best-fit model parameters are the 16th and 84th percentiles of the posterior distributions in the final 10% of the walkers, as shown in Table C.1.

4. Results

4.1. Dust images

Figure 1 presents a multi-wavelength observational overview of HD 34700A. Panel (a) shows the infrared (IR) VLT/SPHERE polarized scattered-light observations and (b) the VLT/ZIMPOL $\text{H}\alpha$ observations of the circumbinary disk, both from Columba et al. (2024). The IR observations exhibit an inner cavity surrounded by a prominent asymmetric ring at $R \approx 0''.50$. Several spiral arms originate from this ring, and it displays an apparent discontinuity or “break” in the north. Inside the IR ring, the $\text{H}\alpha$ -observations display another ring extending from 186 to 335 mas, which traces sub-micron-sized particles (Columba et al. 2024). The $m = 2$ spirals beyond the $\text{H}\alpha$ -ring align with the IR ring, suggesting the IR ring is actually the spirals, albeit at lower angular resolution.

Our new ALMA 225.3 GHz continuum observations in panel (c) reveal a highly asymmetric dust crescent co-located with the IR ring at $0''.39$ (138 au) and an inner unresolved dust disk emission of $55 \mu\text{Jy beam}^{-1}$ ($\sim 11\sigma$), measured by enclosing one beam-size centered on the binary. The continuum emission morphology resembles dust trapped in an anticyclonic vortex (Birnstiel et al. 2013), which is smeared out over the disk’s counterclockwise rotation. A thorough analysis of the continuum emission will be presented in a forthcoming paper (Fasano et al. 2026). A gallery exhibiting the dust emission morphologies is presented in Fig. E.1.

4.2. CO intensity features

The $^{12}\text{CO } J = 2 - 1$, $^{13}\text{CO } J = 2 - 1$, and $\text{C}^{18}\text{O } J = 2 - 1$ zeroth and peak intensity (eighth) moment maps using the robust 1.5 cubes shown in the middle and lower row of Fig. 1, respectively. These moment maps were computed using `bettermoments` (Teague & Foreman-Mackey 2018), with a 2σ clip applied to the data. The peak line emission of ^{12}CO , ^{13}CO , and C^{18}O are $[60.9, 32.7, 10.9] \text{ mJy beam}^{-1}$, respectively. All three CO isotopologs exhibit an inner cavity in their emission, with its elliptic shape elongated toward the north-south direction and, thus, it is asymmetric with respect to the disk major axis. We expected C^{18}O to be more optically thin, which would serve as an indication that it is tracing not only the temperature, but also the density variations as well; this, in turn, suggests the presence of a real gas cavity. However, the observed size of the gas cavity ($R \sim 40 \text{ au}$) cannot be explained by the (tidal) truncation of the inner eccentric binary. Its maximal separation is a mere 0.7 au

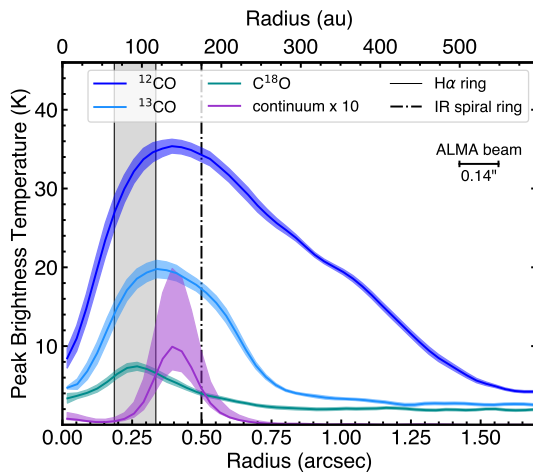


Fig. 2: Brightness temperature radial profiles of CO isotopologs and dust continuum using the high-resolution cubes $0.^{\circ}14 \times 0.^{\circ}11$ (49×39 au) cubes. The latter was multiplied by a factor of 10 to enhance visibility. The colored shaded region shows the standard deviation within each annulus. For the asymmetric continuum emission this traces the pronounced azimuthal variations, rather than an error. The gray-shaded area shows the extent of the $H\alpha$ ring, and the dashed-dotted line shows the peak of the IR ring (values from [Columba et al. 2024](#); [Uyama et al. 2020](#), respectively).

($e_{\text{bin}} = 0.25$, [Torres 2004](#)); hence, it would only have the capacity to carve out a cavity of a maximum size $\leq 6a_{\text{bin}} = 4.2$ au ([Penzlin et al. 2024](#)).

We used the GoFish package ([Teague 2019a](#)) to deproject and azimuthally average the high-resolution peak intensity and continuum maps employing the ^{13}CO geometrical parameters from [discminer](#). We made this choice to ensure a coherent analysis, as the individual best-fit geometrical parameters for the CO isotopologs differ significantly (see Table C.1). We regard the inferred geometry for ^{13}CO as the most reliable because it probes deeper into the disk vertically compared to ^{12}CO , making it significantly less dynamically perturbed. Additionally, it exhibits a higher S/N than C^{18}O , which allows for a more robust fit to the data. For the continuum profile, we further mask the azimuthal regions devoid of emission, which are $[-90, +90]^\circ$ in the disk frame measured from the redshifted major axis. We show the radial emission profiles using the Rayleigh-Jeans approximation to convert to units of K in Fig. 2. The gas cavity is seen across all tracers and its edge is at the inner radius of the $H\alpha$ ring at $R = 0.^{\circ}2$ (65 au) inferred in [Columba et al. \(2024\)](#), as it aligns with the full-width at half maximum (FWHM) of all CO line emission peaks. Interestingly, the C^{18}O emission peak is co-located at the center of the $H\alpha$ ring.

The ^{12}CO peak intensity map in Fig. 1 (g) displays an arc-shaped feature spanning several beam sizes toward the northeast, broadly aligned with a faint spiral arm detected in H-band Q_ϕ (C1; [Columba et al. 2024](#)). Overall, the ^{12}CO emission closely follows the contours of the IR ring, as seen in the ^{12}CO channel maps in Fig. E.2 and the moment 0 map shown in the left panel of Fig. 3. We apply a high-pass filter to the moment 0 map, with the following kernel $\omega(R) = \omega_0(R/1'')^\gamma$ expanding with radius, R , defined in [Speedie et al. \(2024\)](#). We adopted a power-law index of $\gamma = 0.1$ and a kernel width of $\omega_0 = 3$ pixels. The filtered map is then subtracted from the original moment 0 map and the resulting residuals are shown in the right column of Fig. 3. The spatial correlation between positive ^{12}CO filtered residuals and the IR

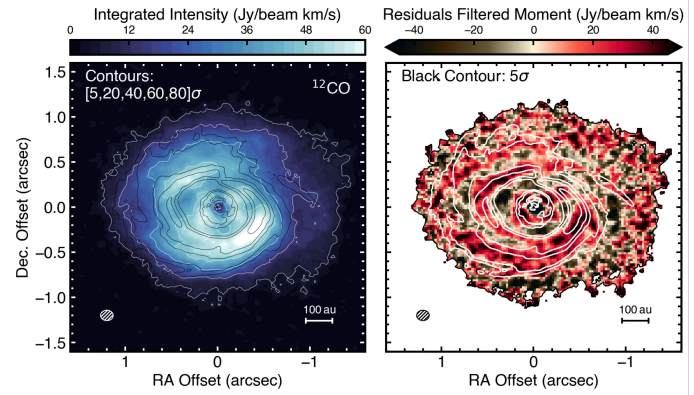


Fig. 3: Line emission features of ^{12}CO . Left: Moment 0 map using the high-resolution cube. Right: Residuals from a moment 0 map subtracted with a high-pass filtered moment map, limited to disk emission above 5σ . The black and white contours in both maps highlight the IR emission, identical to Fig. 1 (a).

ring is striking. It is also noteworthy that there is an asymmetry in the CO emission between the northern and southern sides of the disk; the southern side is brighter, despite it being the side that points away from us (e.g., [Monnier et al. 2019](#)). The southern IR spiral-arc structure corresponds to positive residuals across nearly half of the disk's azimuth. This connection is discussed in more detail in the following sections.

4.3. Gas kinematical diagnostics

4.3.1. Channel maps

In the appendix, we present selected channel maps for the CO isotopologs in Figs. E.2, E.3, and E.4. Again, we overplotted the scattered light contours in the ^{12}CO channel-map gallery. The channel emission exhibits substantial deviations from circular Keplerian rotation, manifesting as spurs that align with the IR ring contours. Along the spiral arms, near the minor axis of the disk, the line emission shows strong vertical (or radial) flows, which we are particularly sensitive to in our (LoS). This causes the emission to shift and spread into adjacent channels, most pronounced on the southern side of the disk. In addition, some of the emission even detaches from the main southern channel wing in channels $4.7 - 5.1 \text{ km s}^{-1}$ seen in Fig. 4. In the following channels ($5.3 - 5.7 \text{ km s}^{-1}$), an extended arc emerges, which is attached to the eastern and southern emission, as well as another spiral feature that now blueshifts the southern emission to the east ($5.7 - 5.9 \text{ km s}^{-1}$). In contrast, the ^{13}CO and C^{18}O channel maps exhibit a smoother emission morphology.

This morphological contrast between ^{12}CO and ^{13}CO and C^{18}O emission can also be seen in the CO channel maps gallery of Figs. E.5–E.7, showing data, [discminer](#) model, and residuals channels together with their peak intensity maps. The complexity of the ^{12}CO emission cannot be captured by the pure Keplerian model, while for ^{13}CO and C^{18}O , the [discminer](#) model describes the emission morphology well.

To further understand the prominent ^{12}CO kinematic features, we utilized the inferred ^{12}CO [discminer](#) geometry (Table C.1) to deproject and plot the position-velocity diagrams for ^{12}CO along the disk axes, as shown in Fig. 5. In the panel displaying the emission along the major axis ($\phi = 0^\circ$), we also overlaid the expected Keplerian rotation and 20% deviations for comparison. The emission is significantly spread

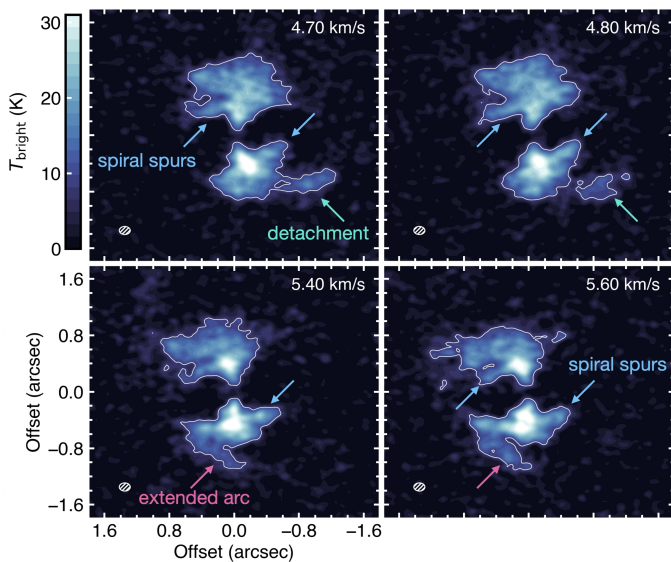


Fig. 4: Selected ^{12}CO channel maps with highlighted non-Keplerian features. White contours enclose 5σ . The beam size of the high-resolution cube employed is shown in the lower left corner and channel id in the upper right corner.

out beyond those limits in velocity space (at approximately $\sim 3 \text{ km s}^{-1}$). However, typical deviations from Keplerian rotation are expected to be on the order of a few percent (i.e., $0.1 \times v_{\text{kep}}(100 \text{ au}) \approx 0.4 \text{ km s}^{-1}$; e.g., Stadler et al. 2025). The broadening of the lines is especially noticeable along the IR ring and its interior. The Keplerian shear within one major beam size (75 au) at this location ($R = 175 \text{ au}$) can reach a maximum of $\Delta v_{\text{kep}} \approx 1 \text{ km s}^{-1}$, which cannot fully account for the observed broadening. The spectral cut along the disk's minor axis ($\phi = 90^\circ$) reveals spread-out emission at radii interior to $\lesssim 300 \text{ au}$. These broad-line widths likely result from rapid and varied radial or vertical motions, which significantly contribute to the LoS velocity (especially at the minor axis). Simultaneously, beam-smearing effects within a few beam sizes from the center can lead to artificial sub-Keplerian rotation and the spreading of emission (e.g., Boehler et al. 2021).

4.3.2. CO spectral analysis

In this subsection, we describe our line profile analysis of the ^{12}CO and ^{13}CO spectra, aimed at gaining further insights into the different velocity structures. First, within the `discminer` analysis framework, we fit a single Gaussian function to the line profile of each pixel to create moment maps for both the data and model cubes, which then trace the line's peak intensity, centroid LoS velocity, and the Gaussian width ($n_{\text{pars}} = 3$). In the center panel of Fig. 6, we present the reduced- χ^2 uncertainty associated with the fit $I_{\text{mom},j}$ to the fiducial ^{12}CO data cube calculated via

$$\chi^2_{\nu} = (n_{\text{ch}} - n_{\text{pars}})^{-1} \sum_j^{n_{\text{ch}}} (I_{\text{d},j} - I_{\text{mom},j})^2 / s_j^2, \quad (2)$$

where s_j is a uniform weighting factor that is the standard deviation of the observed intensity per channel $I_{\text{d},j}$, measured from line-free pixels (Izquierdo et al. 2025).

Dark red colors highlight regions with high fitting uncertainty, where a single Gaussian function provides a poor description of the local line profile. In other words, these regions show

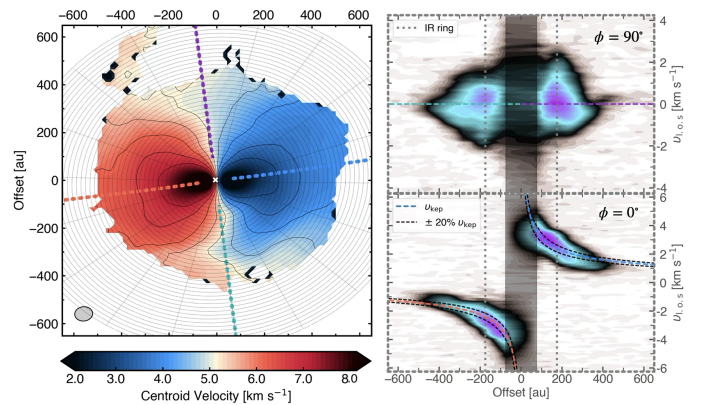


Fig. 5: ^{12}CO position-velocity diagram for fiducial cube. Spectra are extracted along all four angles of the major (red and blue at $\phi = 0^\circ$) and minor (cyan and purple at $\phi = 90^\circ$) disk axes, as highlighted in the Gaussian centroid moment map (left panel). The dashed lines in the PV diagrams (colors corresponding to axes on the left) highlight the disk's Keplerian rotation. The gray shaded areas mask one major beam size in radius from the center. In the $\phi = 0$ panel, the enclosing black dashed lines correspond to 20% deviations from Keplerian rotation. The location of the IR ring ($R = 175 \text{ au}$) is plotted in gray dotted lines in both PV diagrams.

the blend of multiple (spatially) unresolved velocity flows. We extract the local ^{12}CO line profiles at these locations, highlighted by the numbers overplotted on the χ^2 -map. The ^{13}CO spectra are shown to facilitate comparison with the underlying disk rotation (panels 1-3, 6, and 9-12). Panel 1 illustrates a spectrum with low fitting uncertainty, indicating that in these regions, a Gaussian fit (orange line) provides an accurate description of the data.

The map shows a local increase in the reduced- χ^2 in the southeastern part of the disk (panels 6-10). It reveals a secondary component in the line spectra (left peak), offset by over 1 km s^{-1} in its LoS velocity (v_{los}) from the disk component (right peak). This additional component cannot be due to the disk's backside emission, since it should not be visible on the southern side, pointing away from us. We note the spatial co-location of these features with the southeastern IR spirals. The map further displays prominent fitting uncertainties in the disk regions (panels 2, 3, 11, and 12 at $R \approx 190 \pm 10 \text{ au}$) co-located with the asymmetric IR ring and $\text{H}\alpha$ spirals. At these locations, the line spectra exhibit shoulders in addition to the underlying Keplerian rotation outlined by the ^{13}CO spectra. Lastly, the spectra in panels 4 and 5 show the motion of the arc-shaped feature in the northeast. While this feature does not appear to move at smaller radii, the spectrum at pixel 4 exhibits a slight redshift (by a few hundred m s^{-1}) in the v_{LSRK} , indicating that this structure is moving away from us, in line with the expected disk rotation in these regions. In the following discussion, we discuss our interpretation of these secondary line components and shoulders as "exodisk" (following Speedie et al. 2025) material detached from the disk, which is infalling toward the disk in our LoS (redshifted w.r.t. v_{LSRK}).

4.3.3. Residuals from Keplerian rotation

The best-fit `discminer` models applied to each isotopolog (Table C.1) ultimately determined significantly varying disk inclinations and stellar masses among the individual tracers. These findings suggest that the disk may be warped, which we discuss in more detail later in this work. Thus, to accurately compare

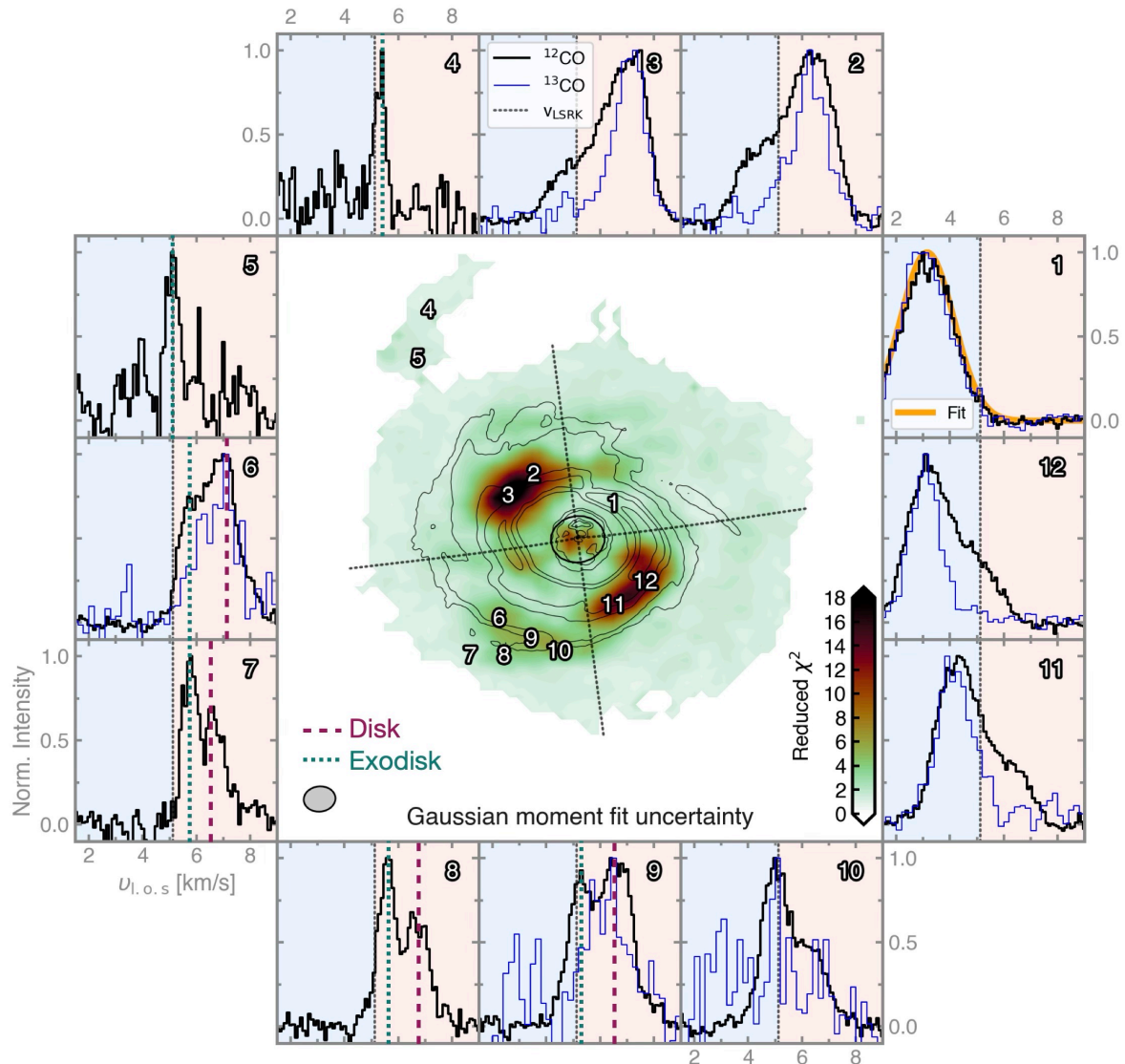


Fig. 6: Line spectra diagnostics. Selected ^{12}CO (black) and ^{13}CO (blue) spectra normalized to their peak extracted at disk locations marked in the center map. The map shows the reduced- χ^2 values (Eq. 2) from the Gaussian moment map fit to the line profile (see accurate fit in panel 1), masked at 5σ . High uncertainties indicate non-Gaussian-shaped line profiles. The line profiles are split by the v_{LSRK} into regions that are either blue- or redshifted to the systemic velocity. Pixels 6-9 that exhibit secondary components in their spectra that are tracing an “exodisk” line component (cyan vertical lines), in addition to the underlying rotating disk component (purple lines). The black contours show the IR scattered light as in Fig. 1 (a) and the dotted lines highlight the disk’s minor and major axes.

the residual maps between the tracers, we re-run another two models for ^{12}CO and C^{18}O cubes, while fixing the geometry (offset, i , PA, v_{LSRK}) to the best-fit ^{13}CO parameters. This ensures that the resulting residuals between the tracers are not due to their different fitted geometric properties. A similar approach was applied in the exoALMA analysis (Izquierdo et al. 2025), using the ^{12}CO best-fit geometric parameters as reference. In our case, we regard the inferred ^{13}CO geometry as more trustworthy compared to the perturbed ^{12}CO kinematics and low S/N emission of C^{18}O . Moreover, fitting the continuum visibility with a model that includes a ring and an asymmetry yielded an inclination and position angle consistent with the kinematic fit of ^{13}CO (Fasano et al. 2026).

Figure 7 shows the Gaussian LoS centroid maps for the data (left panels), model (center panels), and residuals from Keplerian rotation (right panels) for all three isotopologs. The previous sections indicated that the ^{12}CO residuals exhibit highly non-

Keplerian motions. Indeed, spiral spurs are visible, outlining the IR ring (shown in gray contours). We also observed strong non-Keplerian residuals in ^{12}CO at the location of the secondary line components to the southeast and a prominent red- (blue-) shifted pattern at the disk edges to the southwest (northeast). This pattern is further discussed later in this work in relation to disk warping. We additionally present the ^{12}CO centroid residuals, determined by the LoS velocity from the channel of peak intensity shown in the “quadratic” moment maps in Fig. E.8.

The ^{13}CO residuals show a blue or red lobe in the innermost regions, which can be attributed to sub-Keplerian rotation caused by the pressure gradient inside the gas cavity. Beyond a radius of approximately $R \approx 0''.5$, the residual pattern changes to reveal a tentative symmetric blue- or redshift ($\lesssim 0.1 \text{ km s}^{-1}$) along the disk’s minor axis, which might indicate a transition to super-Keplerian rotation coinciding with the IR and continuum ring. In contrast, the C^{18}O residuals are difficult to interpret due to

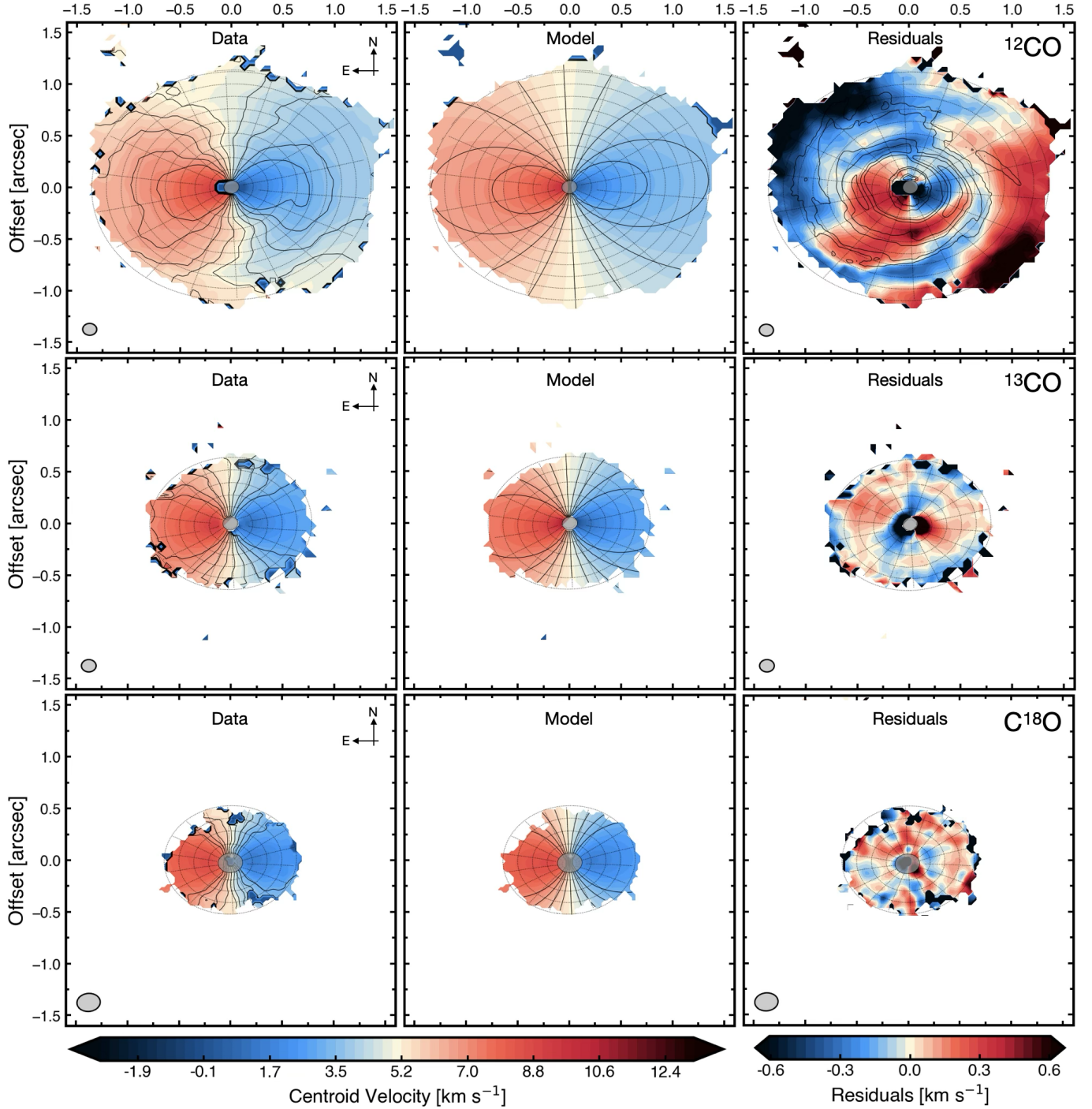


Fig. 7: Gas kinematics for the CO molecular lines. Centroid LoS Gaussian moment maps for the data (left columns), Keplerian model (center columns), and data-model residuals (right columns), for the ^{12}CO (top) and ^{13}CO (middle) data, using high-resolution cubes. The geometry of ^{12}CO and ^{13}CO models was fixed to the ^{13}CO disk, which is less perturbed and has a higher S/N than C^{18}O . For C^{18}O (bottom), we employ the fiducial cube. The respective beam sizes are shown in the lower left corners. In ^{12}CO -residuals, we overplotted the IR contours from Fig. 1(a). All panels share the same scale, color bars, and are masked at 4σ of their peak intensity map. The innermost beam size is masked in as it was excluded from the fit.

their patchy nature, presumably arising from this line's low S/N (see Table A.2).

4.3.4. Vortex kinematics

In this section, we focus on the kinematical patterns around the dust crescent. In Fig. 8, we zoom in on the velocity residuals of ^{13}CO , emphasizing the dust continuum emission with overplotted contours. The red-blue velocity residual pattern co-located with the dust crescent has a magnitude of $\sim \pm 0.10 \text{ km s}^{-1}$. Fol-

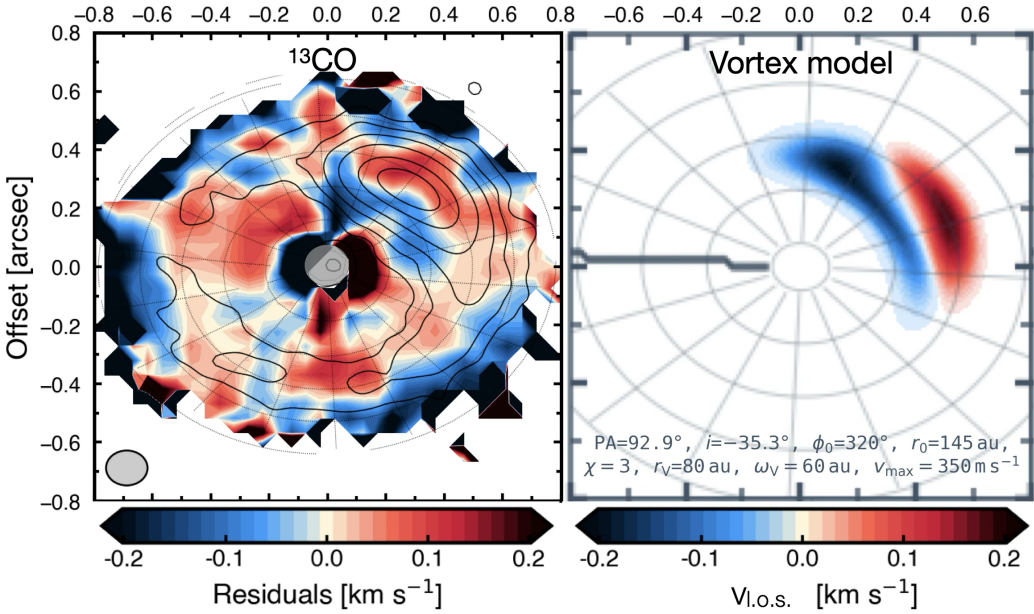


Fig. 8: Vortex kinematics. Left: Centroid residuals for ^{13}CO with overplotted continuum contours the same as in Fig. 1(c). Right: Line-of-sight velocities of the qualitatively best-matching vortex model (Wölfer et al. 2025) with parameters at the bottom. Layout is the same as in Fig. 7.

lowing Appendix B in Teague et al. (2022), we can estimate the significance of these residual velocities based on how accurately we can determine the line centroid from our observations. We measured a Gaussian width of $\Delta V = 0.8 \text{ km s}^{-1}$ and $\text{S/N} \approx 12$ for the ^{13}CO line co-located with the dust crescent. This allows us to determine the accuracy of our line centroid fitting to about one-fifth of a channel, or $\delta v_0 \approx 0.04 \text{ km s}^{-1}$ (see Fig. 13 in Teague et al. 2022). As a result, the observed residuals at the crescent are not significant, with a significance level of only $\sigma = 0.10/0.04 \approx 2.5$. To improve on this result, observations at higher sensitivity and spectral resolution are needed to better sample the velocities at the crescent's location.

Still, we want to assess if this tentative residual pattern is suggestive of anticyclonic motions. Hence, we set up an analytical vortex model presented in Wölfer et al. (2025), similar to the one developed by Robert et al. (2020) and Boehler et al. (2021), to assess whether the ^{13}CO velocity residuals pattern is indicative of an anticyclonic vortex. This model describes the vortex with elliptic streamlines of constant velocity and a Gaussian velocity profile. It incorporates input parameters such as the radial, r_0 , and azimuthal, ϕ_0 , locations of the vortex center, its Gaussian width, ω_v , its aspect ratio χ (for $\chi = 1$ it is circular), and the radius, r_v , of the ring of maximum velocity v_{max} , as well as the disk geometry. We anchor the geometrical values following the dust continuum emission morphology.

We present the resulting $v_{\text{l.o.s.}}$ vortex velocities, based on the location of the continuum crescent ($r_0 = 162 \text{ au}$, $\phi_0 = -40^\circ$) and a set of varying vortex parameters (see Fig. E.9). We attempted to fit the vortex model to the ^{13}CO velocity residuals; however, it did not converge. Therefore, we present the model that best qualitatively (i.e., by-eye) aligns with the observed ^{13}CO velocity residuals, as shown in the right panel of Fig. 8. Its vortex model parameters are $\omega_v = 60 \text{ au}$, $\chi = 3$, $r_v = 100 \text{ au}$ and $v_{\text{max}} = 350 \text{ m s}^{-1}$. We do not compare the ^{12}CO residuals in the figure, as they are contaminated by the spiral features along the IR and continuum ring. We also disregard the C^{18}O residuals due to their low sensitivity ($\text{S/N} < 11$) and limited angular

resolution. The ^{13}CO velocity residual patterns are broadly consistent with those observed in the vortex model. This makes HD 34700A an up-and-coming candidate for follow-up observations in deeper layers of the disk, which are less disturbed than its surface, allowing for a better study of vortex kinematics. Compared to two other major dust asymmetries, it is not affected by cloud absorption, unlike IRS 48 (van der Marel et al. 2013), and its dust crescent is located more favorably between the disk's minor and major axes to study radial and azimuthal motions when compared to HD 142527 (Boehler et al. 2021). Finally, the CO molecular lines in HD 34700A do not experience strong continuum extinction at the crescent location, unlike the other systems.

5. Discussion

The circumbinary disk HD 34700A shows multiple spiral arms, signs of asymmetric continuum emission, and a large inner dust cavity. In the following discussion, we interpret our observations to reveal several key findings: 1) a highly asymmetric continuum crescent that an anticyclonic vortex may explain; 2) a gas cavity indicated by CO molecular lines; 3) ^{12}CO line emission and kinematics that align with the scattered light spiral structures; and 4) whose line spectra show components of spirals and infalling material onto the upper layers of the disk's atmosphere.

Previous studies on this system have attempted to understand the nature of the IR spirals of the circumbinary disk, in particular, their different and large opening angles, as well as the apparent “break” in the asymmetric IR ring toward the north (Monnier et al. 2019; Uyama et al. 2020). Monnier et al. (2019) proposed the presence of a massive companion ($50 M_J$) at this location. However, such a companion has not been detected (Columba et al. 2024), and we do not observe any indications of it from our gas kinematics observations at this location, due to the absence of strong, clustered, high-variance deviations from Keplerian rotation (e.g., Izquierdo et al. 2021). We suggest that the break in the IR ring results from a geometrical view-

ing effect. The IR ring consists of several spiral arms that extend out of the plane, as observed in the $\text{H}\alpha$ image (Columba et al. 2024). Because the northern side of the disk is tilted toward us (Monnier et al. 2019), it appears as if the two ends of the spirals are connected at the same radius, even though they are not likely to be in the same vertical plane (see Fig. E.1 d).

We propose that the spirals and the ring observed in IR emission may indicate the presence of infalling material in the upper layers of the disk. Co-located with the IR ring, we can identify shoulders in the ^{12}CO line spectra (shifted by a few km s^{-1}), as highlighted by the high reduced χ^2 values in Fig. 6. These shoulders are likely dominated by strong downward vertical motions of a few km s^{-1} , as indicated by pixels 2 and 3 being blueshifted and pixels 11 and 12 being redshifted. We consider the radial and azimuthal motions as physically unlikely, since when they are deprojected (divided by $\sin(i_0) \approx 35^\circ \approx 0.6$), they would equate to motions in the disk plane of over 5 km s^{-1} .

Recent hydrodynamical simulations, by Calcino et al. (2025a), have shown that such infall streamers drive long-lived ($\sim 10^4$ yr) super-Keplerian and stationary spiral arms of varying pattern speeds in the disks. Dullemond et al. (2019) also suggested that clouddlet captures can create second-generation transition disks to explain their large cavities, which are generally otherwise hard to reproduce with just one massive companion. Such disks would also be expected to be warped in their outer regions, since the angular momentum of the infalling material is misaligned with the initial disk structure. The significant differences in derived best-fit inclination and PA between each CO isotopolog (see Table C.1) might hint toward a warp in HD 34700A that could help explain the prominent red and blue residual patterns in ^{12}CO (Fig. 7), which appear beyond the IR contours and are nearly symmetrical around the disk's minor axis. A warp is characterized by changes in PA and inclination with radius. However, there are degeneracies between these geometric parameters and any real azimuthal or radial velocity perturbations that may still be present (Rosenfeld et al. 2014).

We present a fit to the ^{12}CO velocity residuals using a simple warped disk model by Winter et al. (2025) with radially varying inclination and position angle in Appendix D. We find a maximal nominal tilt of the disk of $\beta_{\text{max}} = 8.70^\circ \pm 0.27^\circ (\pm 1\sigma)$. As can be seen in Fig. D.1, the warp model reproduces the outermost disk regions beyond 350 au well, which exhibit a $m = 1$ pattern in their centroid residuals. We expect the damping timescales of the warp's bending waves to be on the order of $\tau_{\text{damp}} \sim 1/\alpha \Omega_k$ (Ogilvie & Lubow 2002; Ogilvie & Latter 2013). At $R = 400$ au and for $\alpha = 10^{-3}$ around $M_\star = 4M_\odot$, this results in a relatively long-lived warp of $\tau_{\text{damp}} \approx 4$ Myr. However, the more complex non-Keplerian features observed cannot be explained solely by the warp and are likely influenced by other dynamic processes, such as infall or a massive companion, potentially shaping this disk.

Our CO spectral analysis suggests the presence of additional non-disk-like (exodisk) velocity components, which we interpret as resulting from infalling gas streamers. Anisotropic infall has also been shown to trigger the RWI in disks and generate vortices in hydrodynamical simulations (Bae et al. 2015; Kuznetsova et al. 2022). Vortices are preferably formed near the radial locations of the infall zone, where the accretion streams hit the disk. We cannot state exactly where the potential streamers in the southeast and northeast hit the disk. In the south, it likely merges with the disk at the localized super-Keplerian ^{12}CO residual feature located in the southern part of the IR ring (see Fig. 7 and panels 9 and 10 Fig. 6). We are uncertain about where the structure detected in the northeast con-

nects with the disk, specifically whether it is at the front or the back. This structure might be a remnant of the infall. Further observations of shock-tracing molecules such as SiS and SiO, commonly employed in Class O/I sources (e.g., Podio et al. 2017; Oya et al. 2019; Tychoniec et al. 2021), or SO can help pinpoint these merging zones (van Gelder et al. 2021), as recently employed in the disk of AB Aur (Speedie et al. 2025). Interestingly, both transition disks share many similarities, including a cavity in the IR from which several spiral arms emanate, signs of infalling material, and a continuum ring with a strong asymmetry (Tang et al. 2012, 2017; Calcino et al. 2025b). The continuum crescent of HD 34700A also closely resembles that of IRS 48 (van der Marel et al. 2013; Yang et al. 2023) and HD 142527 (Boehler et al. 2017), the most asymmetric continuum disks observed to date. HD 142527 has a detected M dwarf companion (Lacour et al. 2016; Nowak et al. 2024) and theoretical works suggest the presence of a massive close-in companion in IRS 48 to reproduce its observed features (van der Marel et al. 2013; Calcino et al. 2019). These parallels suggest that similar mechanisms might be at work shaping all three of these disks.

Another discussed scenario of the development of the spiral features is the flyby of one of HD 34700A's stellar companions. Three-dimensional hydrodynamic simulations indicate that flybys can trigger the formation of spiral arms that last for several dynamical timescales, which limits the temporal window for a close encounter to a several tens of thousands of years at most (Smallwood et al. 2023; Cuello et al. 2019, 2023). Flybys primarily induce $m = 2$ spiral arms (e.g., Kurtovic et al. 2018) and both their pattern speed and pitch angles decay quickly over time. By analyzing Gaia DR3 proper motion measurements, Shuai et al. (2022) found a stellar flyby within the past 10^4 yr for HD 34700A unlikely. The closest approach ($d \approx 3000$ au $\approx 9.0^\circ$) was that of HD 34700C (not B); however, we did not detect any disk around it. Furthermore, the most extended spiral arms observed in the IR display very large opening angles ($\sim 30^\circ$ Columba et al. 2024), which should have already wound up, given an optimistic flyby scenario (Smallwood et al. 2023). Lastly, theoretical studies suggest that flybys can cause disks to tilt and warp, yet the timescale of misalignments is too short-lived to explain the observations (Nealon et al. 2020).

Furthermore, the question remains of what causes the innermost gas cavity. Its edge can be placed inside the $\text{H}\alpha$ ring at 0.20° (65 au), which aligns with the CO line emission drop, although the short-separation binary is not able to carve out such a large cavity (Penzlin et al. 2024). Monnier et al. (2019) suggested the possibility of another companion, located between the outer IR ring and the gas cavity, with current detection limits of a few Jupiter masses (Uyama et al. 2020; Columba et al. 2024). Moreover, more massive companions within the gas cavity might be obscured by the coronagraph ($r = 92.5$ mas ≈ 32 au, Columba et al. 2024). These companions ought to be sub-stellar, with masses $\lesssim 30 M_J$, with further evidence provided by the upper limits from the binary's astrometric proper motion anomaly (Vioque et al. 2025).

Our kinematic analysis shows strong residuals from Keplerian rotation (Fig. 7 and 8) interior of the continuum and IR ring ($R < 0.46^\circ \approx 160$ au) of the order of a few 100 m s^{-1} . However, they are not straightforward to interpret; ^{12}CO traces regions high up in the disk atmosphere, which is disturbed by the non-Keplerian motions of the spirals and the potentially infalling material. Nonetheless, the Keplerian deviations, seen as spiral spurs in the channel maps, are substantial along and inside the IR ring ($\sim 2 \text{ km s}^{-1}$, Fig. 5). They display several abrupt changes in Keplerian rotation (blue- and redshifted patterns), called Doppler-

flips, which potentially indicate the location of massive companions (Pérez et al. 2018). However, subtracting a circular Keplerian model from highly non-Keplerian motions observed in an asymmetric, potentially warped, and eccentric disk can result in artificial velocity residuals and Doppler flips (Norfolk et al. 2022; Ragusa et al. 2024).

6. Conclusions

In this paper, we present the first high-resolution ALMA Band 6 observations of the dust continuum and the ^{12}CO , ^{13}CO , and C^{18}O $J = 2 - 1$ line emission of the circumbinary disk around HD 34700A. Our key findings and conclusions are as follows.

- i) The dust continuum observations reveal a highly asymmetric dust crescent on top of a ring at $0\farcs39$ (138 au) located at the edge of a cavity identified by IR observations (Monnier et al. 2019; Columba et al. 2024). We further detected an unresolved inner disk co-located with the central binary at an 11σ significance level.
- ii) The peak intensity maps of all CO isotopologs display an inner gas cavity of $R \approx 65$ au. The ^{12}CO emission is highly structured and asymmetric, with the disk's southern part being brighter than its northern part. Its peak intensity exhibits a detached arc-shaped feature in the northeast and emission substructures that follow the spiral structures observed in the IR.
- iii) The ^{12}CO kinematics shows strong non-Keplerian flows in the form of spiral spurs, which closely follow the IR ring, along with pronounced red- and blueshifted residuals at the disk's southwestern and northeastern edges. The emission morphology of the ^{13}CO and C^{18}O channel maps indicates that emissions from these isotopologs are less dynamically perturbed.
- iv) We found varying disk position angles ($\Delta\text{PA}_{18-12} \approx 3^\circ$) and inclinations ($\Delta i_{18-12} \approx 10^\circ$) inferred from the best-fit Keplerian models between C^{18}O and ^{12}CO . This could indicate that the disk is warped, further supported by our warp model fit (Winter et al. 2025) to the ^{12}CO velocity residuals, which gives a maximum nominal tilt of the disk of $\beta_{\text{max}} = 8.7^\circ \pm 0.3^\circ$.
- v) At the position of the continuum crescent, the ^{13}CO velocity residuals show tentative signs of an anticyclonic vortex when compared to an analytical model (Wölfer et al. 2025). Future molecular line observations of brighter midplane tracers, combined with detailed hydrodynamic simulations, will help in determining whether a vortex would indeed be responsible for these observed residuals.
- vi) The line spectra analysis of ^{12}CO reveals a streamer above the southeastern disk plane, seen as a secondary component to its line profile, with its peak offset by over 1 km s^{-1} . This infalling material may have triggered the Rossby Wave instability (RWI) at the cavity's edge (Bae et al. 2015; Kuznetsova et al. 2022), creating the potential vortex observed in the gas kinematics. Although we cannot pinpoint where this streamer hits the disk at present, future observations of chemical shock tracers, such as SO, can aid in identifying these locations (e.g., Speedie et al. 2025).

The nature of the depleted gas cavity remains a challenge. Our kinematic observations have not definitively pinpointed whether companions are responsible for shaping this cavity. We also speculate that HD 34700A might host a second-generation disk that captured a cludlet (e.g., Kuffmeier et al.

2020). Consequently, this material may not have had sufficient time to accrete onto the binary ($\log(\dot{M}_{\text{acc}}/M_\odot \text{ yr}^{-1}) = -6.8$; Wichitanakom et al. 2020), leading to the formation of the gas cavity. Future ALMA observations of brighter midplane tracers at higher resolution could help elucidate the complex kinematics of the cavity and the existence of an anticyclonic vortex.

Acknowledgements. The authors would like to thank the anonymous referee for the constructive feedback that enhanced the quality of this work. We also thank Alex Ziampiras, Aleksandra Kuznetsova, Clement Baruteau, Enrico Ragusa, John Ilee, and Nicolás Cuello for their helpful discussions. We thank Gabriele Columba for providing the $\text{H}\alpha$ fits file, and Christian Ginski for the DESTINYs fits file and helpful comments. This project has received funding from the European Research Council (ERC) under the European Union's Horizon 2020 research and innovation programme (PROTOPLANETS, grant agreement No. 101002188). JS has performed computations on the 'Mesocentre SIGAMM' machine, hosted by Observatoire de la Côte d'Azur, and acknowledges assistance from Allegro, the European ALMA Regional Center node in the Netherlands. AJW has been supported by the Royal Society through a University Research Fellowship grant number URF/R1/241791. Support for AFI was provided by NASA through the NASA Hubble Fellowship grant No. HST-HF2-51532.001-A awarded by the Space Telescope Science Institute, which is operated by the Association of Universities for Research in Astronomy, Inc., for NASA, under contract NAS5-26555. JeS acknowledges financial support from the Natural Sciences and Engineering Research Council of Canada (NSERC) through the Canada Graduate Scholarships Doctoral (CGS D) program, and from the Heising-Simons Foundation through the 51 Pegasi b Fellowship. JB acknowledges support from NASA XRP grant No. 80NSSC23K1312. SF is funded by the European Union (ERC, UNVEIL, 101076613). SF acknowledges financial contribution from PRIN-MUR 2022YP5ACE. This paper makes use of the following ALMA data: ADS/JAO.ALMA#2022.1.00760.S. ALMA is a partnership of ESO (representing its member states), NSF (USA), and NINS (Japan), together with NRC (Canada), NSC and ASIAA (Taiwan), and KASI (Republic of Korea), in cooperation with the Republic of Chile. The Joint ALMA Observatory is operated by ESO, AUI/NRAO, and NAOJ.

Software: `analysisUtils` (Hunter et al. 2023), `Bettermoments` (Teague & Foreman-Mackey 2018), `CARTA` (Comrie et al. 2021), `CASA` (McMullin et al. 2007; CASA Team et al. 2022), `Discminer` (Izquierdo et al. 2021), `emcee` (Foreman-Mackey et al. 2013, 2019), `GoFish` (Teague 2019a), `Matplotlib` (Hunter 2007), `Numpy` (van der Walt et al. 2011), `reduction_utils` scripts by the DSHARP and MAPS ALMA Large Programs (Andrews et al. 2018; Czekala et al. 2021), `Scipy` (Virtanen et al. 2020).

References

Akeson, R. L., Rice, W. K. M., Boden, A. F., et al. 2007, *ApJ*, 670, 1240
 Andrews, S. M., Huang, J., Pérez, L. M., et al. 2018, *ApJ*, 869, L41
 Artymowicz, P. & Lubow, S. H. 1994, *ApJ*, 421, 651
 Bae, J., Hartmann, L., & Zhu, Z. 2015, *ApJ*, 805, 15
 Bae, J., Zhu, Z., & Hartmann, L. 2016, *ApJ*, 819, 134
 Benac, P., Matrà, L., Wilner, D. J., et al. 2020, *ApJ*, 905, 120
 Birnstiel, T., Dullemond, C. P., & Pinilla, P. 2013, *A&A*, 550, L8
 Boehler, Y., Ménard, F., Robert, C. M. T., et al. 2021, *A&A*, 650, A59
 Boehler, Y., Weaver, E., Isella, A., et al. 2017, *ApJ*, 840, 60
 Bracco, A., Chavhan, P. H., Provenzale, A., & Spiegel, E. A. 1999, *Physics of Fluids*, 11, 2280
 Briggs, D. S. 1995, PhD thesis, New Mexico Institute of Mining and Technology
 Calcino, J., Norfolk, B. J., Price, D. J., et al. 2024, *MNRAS*, 534, 2904
 Calcino, J., Price, D. J., Hilder, T., et al. 2025a, *MNRAS*, 537, 2695
 Calcino, J., Price, D. J., & Ormel, C. W. 2025b, *ApJ*, arXiv:2510.05601
 Calcino, J., Price, D. J., Pinte, C., et al. 2023, *MNRAS*, 523, 5763
 Calcino, J., Price, D. J., Pinte, C., et al. 2019, *MNRAS*, 490, 2579
 CASA Team, Bean, B., Bhatnagar, S., et al. 2022, *PASP*, 134, 114501
 Casassus, S., van der Plas, G. M., Perez, S., et al. 2013, *Nature*, 493, 191
 Columba, G., Rigliaco, E., Gratton, R., et al. 2024, *A&A*, 681, A19
 Comrie, A., Wang, K.-S., Hsu, S.-C., et al. 2021, *CARTA: The Cube Analysis and Rendering Tool for Astronomy*, Zenodo
 Cuello, N., Alaguero, A., & Poblete, P. P. 2025, *Circumstellar and Circumbinary Discs in Multiple Stellar Systems*
 Cuello, N., Dipierro, G., Mentiplay, D., et al. 2019, *MNRAS*, 483, 4114
 Cuello, N., Ménard, F., & Price, D. J. 2023, *European Physical Journal Plus*, 138, 11
 Curone, P., Facchini, S., Andrews, S. M., et al. 2025, *ApJL*, 984, L9
 Czekala, I., Loomis, R. A., Teague, R., et al. 2021, *ApJS*, 257, 2
 Dong, R., Fung, J., & Chiang, E. 2016, *ApJ*, 826, 75
 Dullemond, C. P., Kuffmeier, M., Goicovic, F., et al. 2019, *A&A*, 628, A20

Fasano, D., Benisty, M., Stadler, J., & Zagaria, F. 2026, A&A, submitted

Flock, M., Fromang, S., Turner, N. J., & Benisty, M. 2017, ApJ, 835, 230

Flock, M., Ruge, J. P., Dzyurkevich, N., et al. 2015, A&A, 574, A68

Foreman-Mackey, D., Farr, W., Sinha, M., et al. 2019, The Journal of Open Source Software, 4, 1864

Foreman-Mackey, D., Hogg, D. W., Lang, D., & Goodman, J. 2013, PASP, 125, 306

Gaia Collaboration, Vallenari, A., Brown, A. G. A., et al. 2023, A&A, 674, A1

Garufi, A., Ginski, C., van Holstein, R. C., et al. 2024, A&A, 685, A53

Gupta, A., Miotello, A., Manara, C. F., et al. 2023, A&A, 670, L8

Hilder, T., Casey, A. R., Price, D. J., et al. 2025, ApJ, 984, L13

Hirsh, K., Price, D. J., Gonzalez, J.-F., Ubeira-Gabellini, M. G., & Ragusa, E. 2020, MNRAS, 498, 2936

Huang, J., Andrews, S. M., Öberg, K. I., et al. 2020, ApJ, 898, 140

Huang, J., Bergin, E. A., Bae, J., Benisty, M., & Andrews, S. M. 2023, ApJ, 943, 107

Huang, J., Bergin, E. A., Öberg, K. I., et al. 2021, ApJS, 257, 19

Hunter, J. D. 2007, Computing in Science Engineering, 9, 90

Hunter, T. R., Petry, D., Barkats, D., Corder, S., & Indebetouw, R. 2023, analysisUtils

Izquierdo, A. F., Stadler, J., Galloway-Sprietsma, M., et al. 2025, ApJ, 984, L8

Izquierdo, A. F., Testi, L., Facchini, S., Rosotti, G. P., & van Dishoeck, E. F. 2021, A&A, 650, A179

Kuffmeier, M., Dullemond, C. P., Reissl, S., & Goicovic, F. G. 2021, A&A, 656, A161

Kuffmeier, M., Goicovic, F. G., & Dullemond, C. P. 2020, A&A, 633, A3

Kurtovic, N. T., Pérez, L. M., Benisty, M., et al. 2018, ApJ, 869, L44

Kurtovic, N. T., Pinilla, P., Penzlin, A. B. T., et al. 2022, A&A, 664, A151

Kuznetsova, A., Bae, J., Hartmann, L., & Mac Low, M.-M. 2022, ApJ, 928, 92

Lacour, S., Biller, B., Cheetham, A., et al. 2016, A&A, 590, A90

Li, H., Finn, J. M., Lovelace, R. V. E., & Colgate, S. A. 2000, ApJ, 533, 1023

Loomis, R. A., Facchini, S., Benisty, M., et al. 2025, ApJ, 984, L7

Lovelace, R. V. E., Li, H., Colgate, S. A., & Nelson, A. F. 1999, ApJ, 513, 805

Marzari, F. & Thebault, P. 2019, Galaxies, 7, 84

McMullin, J. F., Waters, B., Schiebel, D., Young, W., & Golap, K. 2007, in Astronomical Society of the Pacific Conference Series, Vol. 376, Astronomical Data Analysis Software and Systems XVI, ed. R. A. Shaw, F. Hill, & D. J. Bell, 127

Monnier, J. D., Harries, T. J., Bae, J., et al. 2019, ApJ, 872, 122

Nealon, R., Cuello, N., & Alexander, R. 2020, MNRAS, 491, 4108

Norfolk, B. J., Pinte, C., Calcino, J., et al. 2022, ApJ, 936, L4

Nowak, M., Rowther, S., Lacour, S., et al. 2024, A&A, 683, A6

Offner, S. S. R., Moe, M., Kratter, K. M., et al. 2023, in Astronomical Society of the Pacific Conference Series, Vol. 534, Protostars and Planets VII, ed. S. Inutsuka, Y. Aikawa, T. Muto, K. Tomida, & M. Tamura, 275

Ogilvie, G. I. & Latter, H. N. 2013, MNRAS, 433, 2403

Ogilvie, G. I. & Lubow, S. H. 2002, MNRAS, 330, 950

Oya, Y., López-Sepulcre, A., Sakai, N., et al. 2019, ApJ, 881, 112

Penzlin, A. B. T., Booth, R. A., Nelson, R. P., Schäfer, C. M., & Kley, W. 2024, MNRAS, 532, 3166

Pérez, S., Casassus, S., & Benítez-Llambay, P. 2018, MNRAS, 480, L12

Podio, L., Codella, C., Lefloch, B., et al. 2017, MNRAS, 470, L16

Ragusa, E., Alexander, R., Calcino, J., Hirsh, K., & Price, D. J. 2020, MNRAS, 499, 3362

Ragusa, E., Fasano, D., Toci, C., et al. 2021, MNRAS, 507, 1157

Ragusa, E., Lynch, E., Laibe, G., Longarini, C., & Cepi, S. 2024, A&A, 686, A264

Robert, C. M. T., Méheut, H., & Ménard, F. 2020, Astronomy & Astrophysics, 641, A128

Rosenfeld, K. A., Chiang, E., & Andrews, S. M. 2014, ApJ, 782, 62

Shuai, L., Ren, B. B., Dong, R., et al. 2022, ApJS, 263, 31

Smallwood, J. L., Yang, C.-C., Zhu, Z., et al. 2023, MNRAS, 521, 3500

Speedie, J., Dong, R., Hall, C., et al. 2024, Nature, 633, 58

Speedie, J., Dong, R., Teague, R., et al. 2025, ApJ, 981, L30

Stadler, J., Benisty, M., Winter, A. J., et al. 2025, ApJ, 984, L11

Sterzik, M. F., Melo, C. H. F., Tokovinin, A. A., & van der Blieck, N. 2005, A&A, 434, 671

Tang, Y.-W., Guilloteau, S., Dutrey, A., et al. 2017, ApJ, 840, 32

Tang, Y. W., Guilloteau, S., Piétu, V., et al. 2012, A&A, 547, A84

Teague, R. 2019a, The Journal of Open Source Software, 4, 1632

Teague, R. 2019b, Research Notes of the American Astronomical Society, 3, 74

Teague, R., Bae, J., Andrews, S. M., et al. 2022, ApJ, 936, 163

Teague, R., Bae, J., Birnstiel, T., & Bergin, E. A. 2018, ApJ, 868, 113

Teague, R., Benisty, M., Facchini, S., et al. 2025, ApJ, 984, L6

Teague, R. & Foreman-Mackey, D. 2018, Bettermoments: A Robust Method To Measure Line Centroids, Zenodo

Thebault, P. & Bonanni, D. 2025, A&A, 700, A106

Torres, G. 2004, AJ, 127, 1187

Tychoniec, Ł., van Dishoeck, E. F., van't Hoff, M. L. R., et al. 2021, A&A, 655, A65

Uyama, T., Currie, T., Christiaens, V., et al. 2020, ApJ, 900, 135

van der Marel, N., Birnstiel, T., Garufi, A., et al. 2021, AJ, 161, 33

van der Marel, N., van Dishoeck, E. F., Bruderer, S., et al. 2013, Science, 340, 1199

van der Walt, S., Colbert, S. C., & Varoquaux, G. 2011, Computing in Science and Engineering, 13, 22

van Gelder, M. L., Tabone, B., van Dishoeck, E. F., & Godard, B. 2021, A&A, 653, A159

Vioque, M., Booth, R. A., Ragusa, E., et al. 2025, A&A, arXiv:2512.00157

Virtanen, P., Gommers, R., Burovski, E., et al. 2020, scipy/scipy: SciPy 1.5.3

Wichittanakom, C., Oudmaijer, R. D., Fairlamb, J. R., et al. 2020, MNRAS, 493, 234

Winter, A. J., Benisty, M., Izquierdo, A. F., et al. 2025, ApJ, 990, L10

Wölfer, L., Barraza-Alfaro, M., Teague, R., et al. 2025, ApJ, 984, L22

Yang, H., Fernández-López, M., Li, Z.-Y., et al. 2023, ApJ, 948, L2

Young, A. K., Alexander, R., Rosotti, G., & Pinte, C. 2022, MNRAS, 513, 487

Appendix A: Observations, imaging, and emission properties

Table A.1 contains the relevant information of each EB used for the measurement sets and images produced. Table A.2 lists the imaging parameters and emission properties of the continuum and molecular line data cubes for both HD 34700A and B.

Table A.1: Details of all the EBs included in the HD 34700 measurement set.

Date	No. Ant.	Int (min)	Baselines (m)	Resolution (arcsec)	Max. Scale (arcsec)	Phase Cal.	Flux/Bandpass Cal.
2022-10-09	43	50	15-500	0.64	6.97	J0509+0541	J0423-0120
2022-10-09	43	50	15-500	0.64	6.97	J0527+0331	J0423-0120
2023-05-13	42	47	15-2516	0.13	2.12	J0509+0541	J0423-0120
2023-05-19	44	47	78-3638	0.10	1.43	J0509+0541	J0423-0120
2023-05-19	44	47	78-3638	0.10	1.43	J0509+0541	J0423-0120
2023-05-19	44	47	78-3638	0.10	1.43	J0509+0541	J0423-0120
2023-05-21	42	47	28-3638	0.10	1.44	J0509+0541	J0423-0120
2023-05-21	42	47	28-3638	0.10	1.44	J0509+0541	J0423-0120
2023-05-24	42	47	28-3638	0.09	1.41	J0509+0541	J0423-0120
2023-05-28	42	47	28-3638	0.10	1.61	J0509+0541	J0423-0120
2023-05-28	42	47	28-3638	0.10	1.61	J0509+0541	J0423-0120
2023-05-30	42	47	28-3638	0.10	1.44	J0509+0541	J0423-0120
2023-06-02	42	47	28-3638	0.10	1.57	J0509+0541	J0423-0120

Table A.2: HD 34700 imaging parameters and emission properties of various tracers.

Source	Tracer	Freq. (GHz)	Chan. Sp. (km/s)	Rob.	Beam size (mas ²)	PA (deg)	RMS Noise (mJy bm ⁻¹)	Peak int. (mJy bm ⁻¹)	S/N	Int. Flux (mJy)
(1)	(2)	(3)	(4)	(5)	(6)	(7)	(8)	(9)	(10)	(11)
AaAb	Continuum	225.3	1.5	0.5	137 × 115	86.3	5.07 × 10 ⁻³	2.32	458	8.42 ± 0.84
	¹² CO	230.5	0.1	0.5	137 × 115	88.8	1.12	29.9	26.7	4167 ± 42
	¹³ CO	220.4	0.2	0.5	142 × 119	90.1	0.85	18.8	22.1	805 ± 80
	C ¹⁸ O	219.6	0.2	1.5	227 × 175	95.2	0.68	16.9	10.9	123 ± 12
B	Continuum	225.3	1.5	0.5	137 × 115	86.3	5.07 × 10 ⁻³	1.61	318	3.12 ± 0.31
	¹² CO	230.5	0.1	0.5	137 × 115	88.8	1.12	13.1	11.7	106 ± 11

Columns - (1): Source. (2): Tracer. (3): Average observation frequency. (4): Imaged channel spacing. (5): Briggs weighting robust parameter. (6) and (7): Synthesized beam size and PA. (8): RMS noise. (9): Peak intensity. (10): Peak S/N. (11): Integrated flux with 10% flux uncertainty in ALMA Band 6.

Appendix B: Circumstellar disk of HD 34700B

We present an overview plot of the HD 34700 system showing HD 34700A and B in the same field of view in Fig. B.1. We re-detected both continuum and ¹²CO emission co-located with companion B, its peak intensities and integrated fluxes are listed in Table A.2. We did not detect any ¹³CO or C¹⁸O emission ($> 3\sigma$) around B, and no CO molecular line or continuum emission around HD 34700C. In addition, we did not detect any continuum or ¹²CO emission bridging over A to B, even when the data were imaged at lower resolution and higher sensitivity. In Fig. B.2, we show the Band 6 detected continuum and ¹²CO observations centered and zoomed-in on HD 34700B. The LoS velocity (Fig. B.2d) shows the clockwise Keplerian rotation of the disk with a systemic velocity v_{LSRK} similar to that of HD 34700A (colorbar centered on v_{LSRK} of A), confirming that the stars are co-moving. Due to the low S/N and resolution, we did not attempt to fit for ¹²CO emission around B.

Appendix C: Best-fit parameter table

In Table C.1 we show the best-fit `discminer` model parameters of HD 34700A for each CO isotopolog.

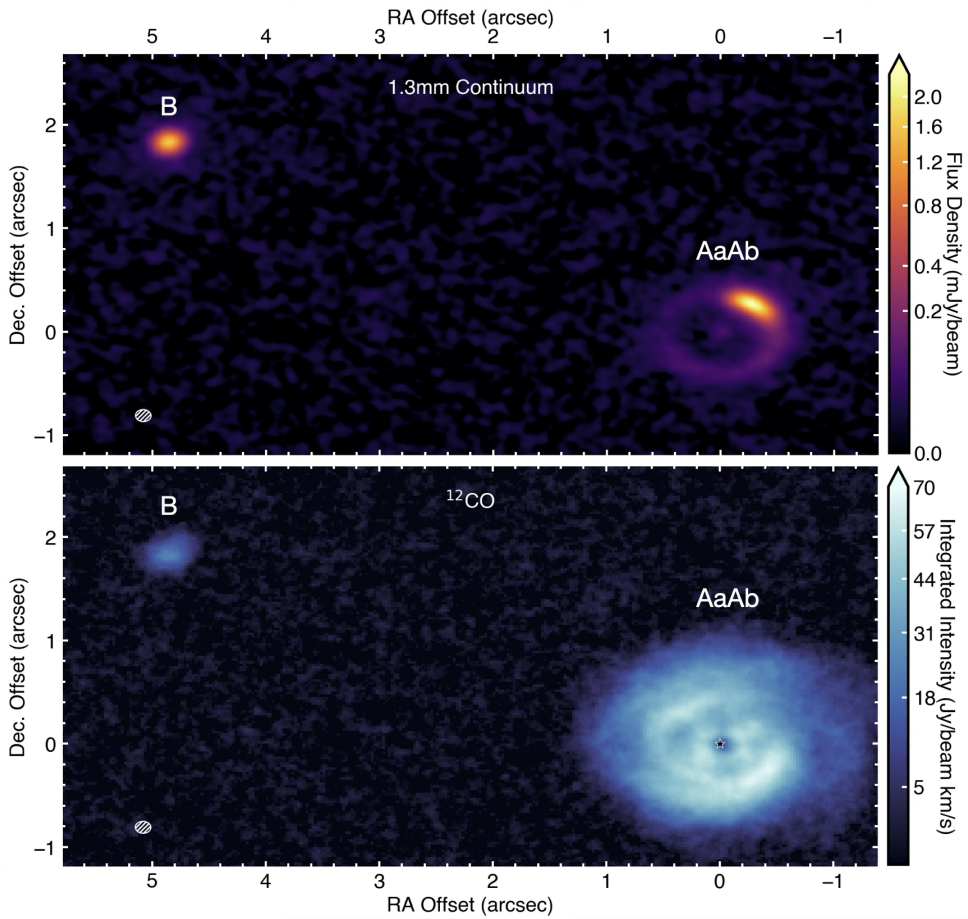


Fig. B.1: Overview plot of HD 34700 AaAb and B. Top: 225.3 GHz dust continuum emission plotted with a power-law scaling of $\gamma = 0.4$ to highlight faint emission. Bottom: ^{12}CO $J = 2 - 1$ moment 0 map. The beam size ($0.^{\circ}14 \times 0.^{\circ}11$) of the robust 0.5 cubes employed is shown in the lower-left corner. No continuum or ^{12}CO molecular line emission was detected bridging both disks around HD 34700A and B, even when the data were imaged at a lower resolution and higher sensitivity.

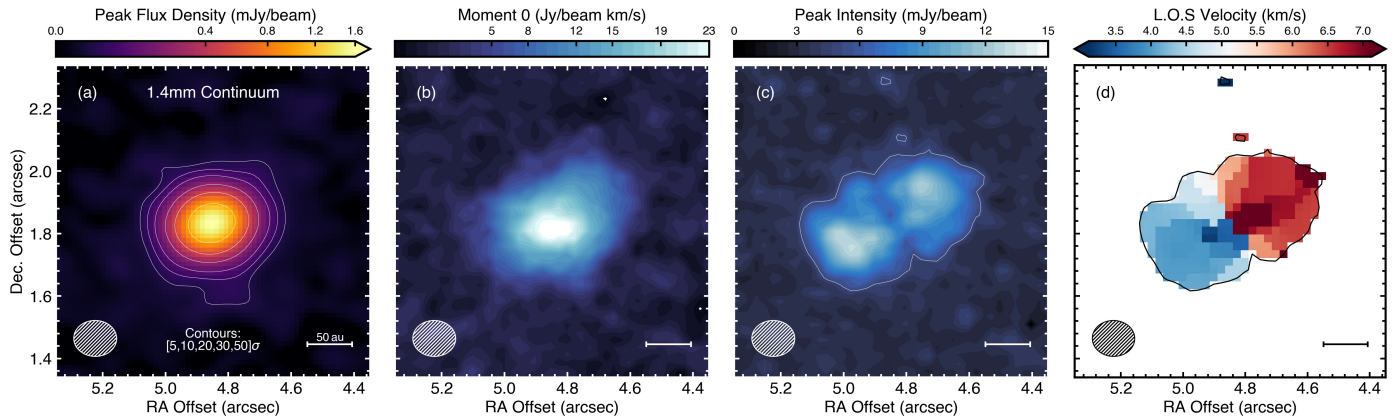


Fig. B.2: Band 6 observation of HD 34700B. (a) 225.3 GHz dust continuum. (b) ^{12}CO moment 0 map. (c) ^{12}CO peak intensity map, white contour encloses 5σ . (d) ^{12}CO LoS quadratic centroid map, masked at 5σ of the peak intensity map. The beam size of the high-resolution cubes employed is shown in the lower left corner.

Appendix D: Warped disk model

Winter et al. (2025) demonstrated that the $m = 1$ LoS velocity residual structure, after subtracting a Keplerian model, can be interpreted as evidence of moderate disk warping. In this section of the appendix, we present an interpretation of the ^{12}CO velocity residuals (Fig. 7) as due to warping of the disk, which means a moderate change of the disk's inclination i_0 and position angle PA with radius. We employ the analytical warp model recently published by Winter et al. (2025) within the exoALMA Large Program paper series (Teague et al. 2025). The model interprets velocity residual motions δv_{los} as primary due to a varying LoS

Table C.1: Best-fit `discminer` model parameters.

Tracer	M_\star (M_\odot)	v_{LSRK} (km s^{-1})	i_0 (deg)	PA (deg)	x_c (mas)	y_c (mas)	z_0 (au)	p	R_t (au)	q
^{12}CO	$4.38_{-0.02}^{+0.02\dagger}$	$5.125_{-0.001}^{+0.002}$	$-30.9_{-0.1}^{+0.1}$	$96.5_{-0.1}^{+0.1}$	-26_{-1}^{+4}	8_{-2}^{+1}	$12.1_{-1.0}^{+0.3}$	$0.34_{-0.01}^{+0.04}$	331_{-11}^{+4}	$1.57_{-0.01}^{+0.01}$
^{13}CO	$4.64_{-0.05}^{+0.04}$	$5.122_{-0.003}^{+0.002}$	$-35.3_{-0.2}^{+0.2}$	$93.0_{-0.1}^{+0.1}$	$-3.1_{-0.7}^{+0.8}$	30_{-2}^{+2}	62_{-3}^{+2}	$0.86_{-0.03}^{+0.03}$	125_{-5}^{+6}	$0.95_{-0.02}^{+0.02}$
C^{18}O	$3.92_{-0.06}^{+0.08\dagger}$	$5.121_{-0.008}^{+0.011}$	$-42.6_{-0.7}^{+0.4}$	$94.0_{-0.3}^{+0.2}$	7_{-2}^{+2}	47_{-26}^{+2}	67_{-27}^{+4}	$0.34_{-0.02}^{+0.03}$	153_{-14}^{+14}	$0.50_{-0.05}^{+0.09}$

The total stellar mass of the binary M_\star , systemic velocity v_{LSRK} , geometrical parameters (x_c, y_c offset from the central binary, PA position angle measured from the North to the redshifted major axis, and negative inclination i_0 indicates anti-clockwise disk rotation), and emission surface parameters (z_0, p, R_t, q describe an exponentially tapered power law) were inferred from the high-resolution cubes for ^{12}CO and ^{13}CO and the fiducial cube for C^{18}O . The reported MCMC uncertainties are represented by the 16th and 84th percentiles drawn from the posterior distribution of the final 10% walkers of each model. These `discminer`-model uncertainties can increase by a factor of ~ 10 due to spatially correlated noise, as shown by Hilder et al. (2025). The strongest correlation between model parameters is observed between the stellar mass and the disk inclination, which are known to be degenerate (e.g. Teague et al. 2018). This $M_\star \cdot \sin i_0$ degeneracy is evident through the varying best-fit parameters among CO isotopologs. Note that the inferred inclinations i_0 and position angles PA between the CO tracers are significantly different, which we interpret as a sign of disk warping.

\dagger Stellar masses for ^{12}CO and C^{18}O models with geometrical parameters fixed to the best-fit ^{13}CO ones are $3.58 M_\odot$ and $5.01 M_\odot$, respectively.

component of the Keplerian rotational velocity $v_\phi(R) = \sqrt{GM_\star/R}$ due to disk warping. We employ the ^{12}CO `discminer` model with geometrical properties fixed to the ^{13}CO , as it most robustly traces the underlying Keplerian disk rotation. Minor changes to the best-fit inclination δi_0 and position angle δPA will then tilt each radial annulus compared to the flat initial LoS velocity $v_{\text{los}}^{\text{flat}}(R, \phi)$. The residuals in the LoS velocity can then be described as

$$\delta v_{\text{los}}(R, \phi) = v_{\text{los}}^{\text{warp}} - v_{\text{los}}^{\text{flat}} = v_\phi(R) [\delta i(R) \cos i_0 \cos \phi + \delta\text{PA}(R) \sin i_0 \sin \phi]. \quad (\text{D.1})$$

The angle ϕ is measured counter-clockwise from the redshifted major axis of the disk ($\phi = 0$). The above equation can also be rewritten in the form

$$\delta v_{\text{los}}(R, \phi) = A(R) \cos \phi + B(R) \sin \phi. \quad (\text{D.2})$$

The warp model then fits the coefficients $A(R)$ and $B(R)$ to each radial annulus of the velocity residual map, which are given by

$$\begin{aligned} \delta i(R) &= \frac{A(R)}{v_\phi(R) \cos i_0}, \\ \delta\text{PA}(R) &= \frac{B(R)}{v_\phi(R) \sin i_0}. \end{aligned} \quad (\text{D.3})$$

We can further define the warp's tilt angle $\beta(R) \approx \sqrt{\delta i(R)^2 + \delta\text{PA}(R)^2 \sin^2 i_0}$ with its maximum value β_{max} interpreted as the tilt amplitude (Winter et al. 2025).

The best-fit warp parameters and the resulting LoS residual map δv_{los} are shown in Fig. D.1. The warp model residual map reproduces the strong $m = 1$ residual pattern in the outermost disk regions beyond 350 au well, represented by changes in disk inclination and position angle of up to 8° from their best-fit values. However, inside 300 au, no clear $m = 1$ patterns are observed, and thus the LoS residuals cannot be explained by warping alone. Overall, there are significant residuals between the observed data and the warped model. Other dominant dynamics, such as infall, likely drive these differences. Since the model attributes the entire LoS velocity difference (δv_{los}) to warping, it is likely that the warp's tilt (β) and amplitude (ψ) are overestimated.

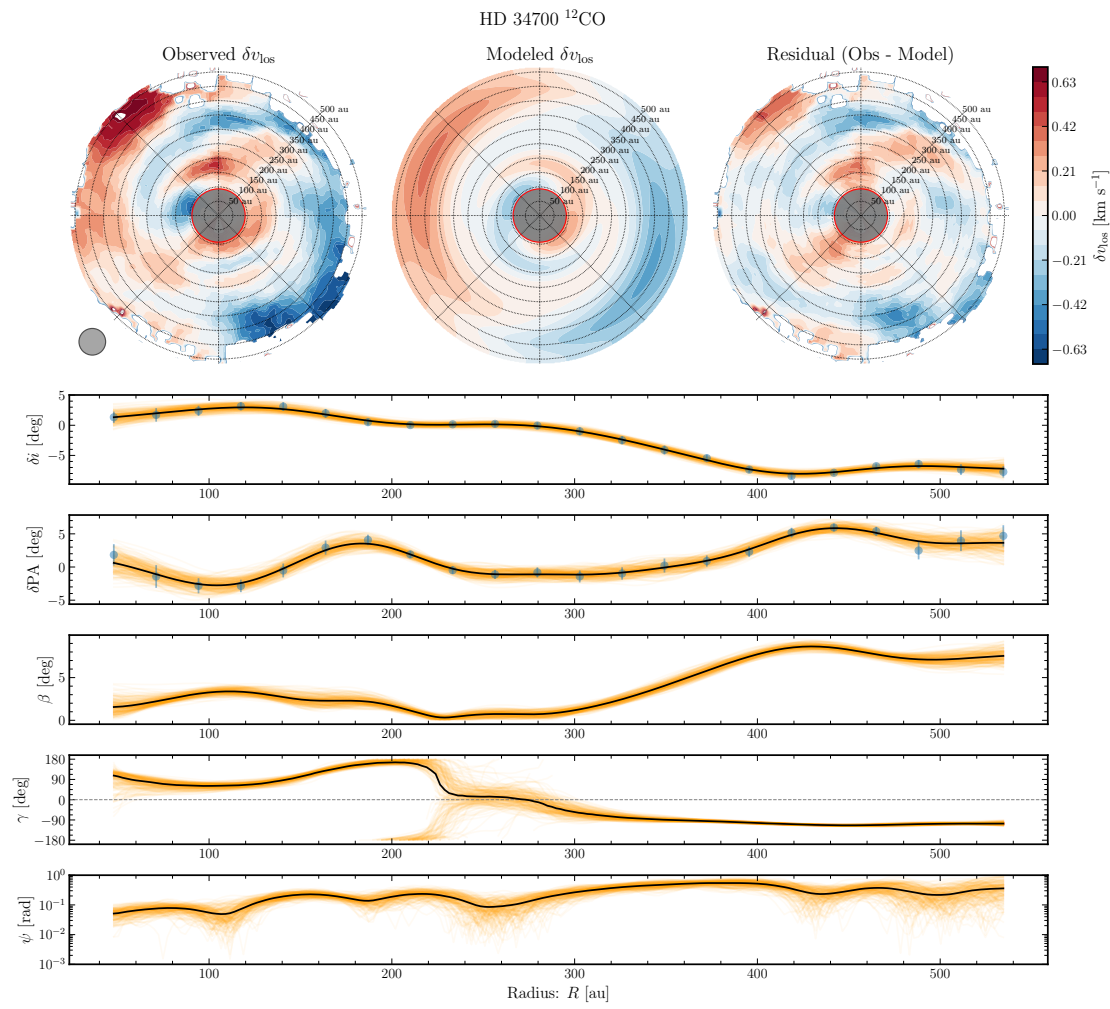


Fig. D.1: Warped disk model for ^{12}CO HD 34700A. Top panels: Residuals (right) from the observed (left) vs modeled (center) δv_{los} fields for HD 34700A after fitting Keplerian velocity profiles. The color scale δv_{los} in km/s is identical in all panels. Grey circles mask twice the central beam size. The beam size ($0.14'' \approx 50$ au) is also shown on the left-hand side, assumed to be circular for visualization. Bottom panels: Radial profiles of δi , δPA , and the physical warp properties tilt β , twist γ , and the warp amplitude ψ from our fitting procedure (Eqs. 13-15 in Winter et al. 2025). Blue points and error bars in δi and δPA come from the least-squares fitting procedure. Faint orange lines show posterior distributions from a Gaussian process model.

Appendix E: Complementary figures

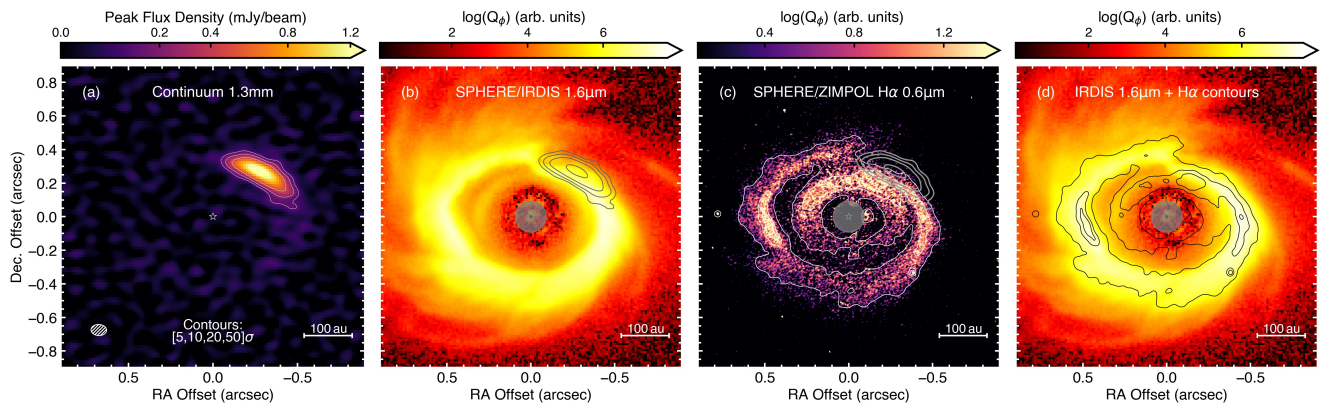


Fig. E.1: Gallery of HD 34700A dust images. (a) High-resolution (92×66 mas 2) 225.3 GHz dust continuum. (b) SPHERE/IRDIS IR scattered light observations and (c) SPHERE/ZIMPOL H α observations presented in Columba et al. (2024), with the gray circles representing the coronograph ($r = 92.5$ mas ≈ 32 au). Overlaid dust continuum contours are the same as in (a). (d) IR scattered light observations with H α contours of (c).

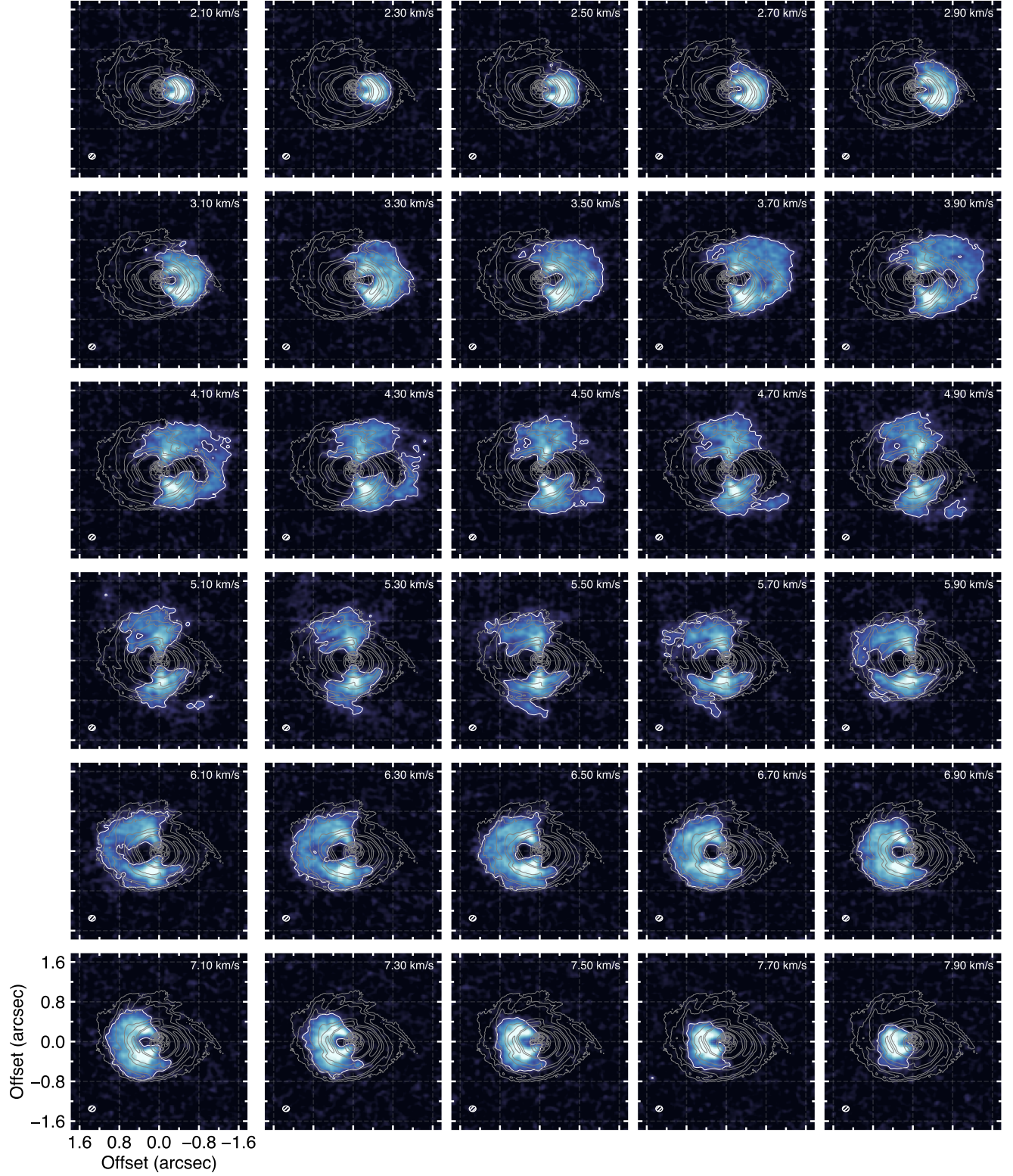


Fig. E.2: Channel maps for the ^{12}CO $J = 2 - 1$ molecular line. The white contour enclosing the line emission shows 5σ . The gray background contours indicate the scattered light emission, same as Fig. 1 (a), to highlight that the spiral spurs in the line emission closely follow the IR ring. The beam size of the high-resolution cube is plotted in the lower left corner. Note that we only show every second channel (200 m s^{-1}), and the systemic-velocity channel is at 5.1 km s^{-1} . A movie of the ^{12}CO channel maps can be found in the online resources.

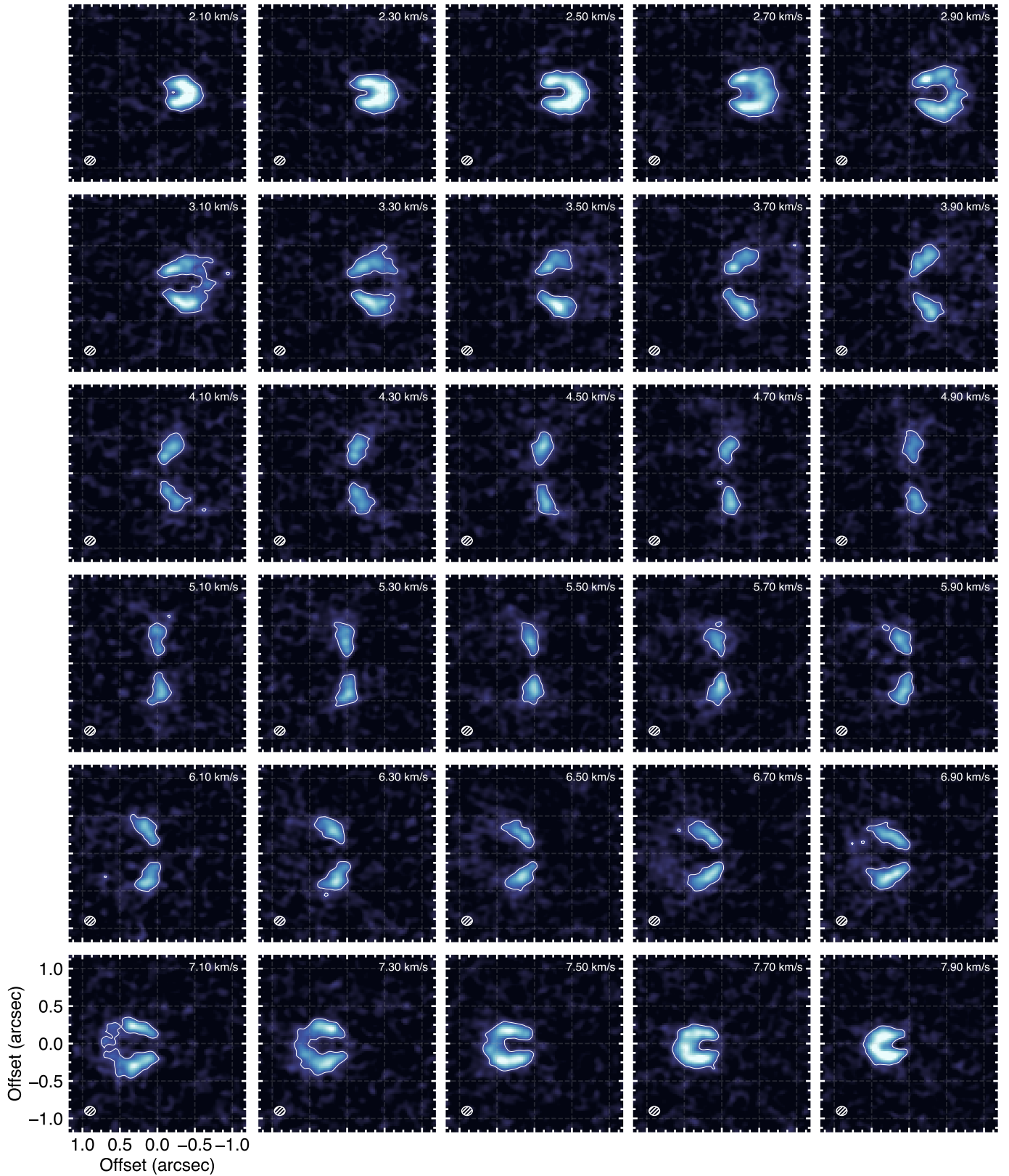


Fig. E.3: Same as Fig. E.2 but for the ^{13}CO $J = 2 - 1$ molecular line high-resolution cube imaged at a channel spacing of 200 m s^{-1} .

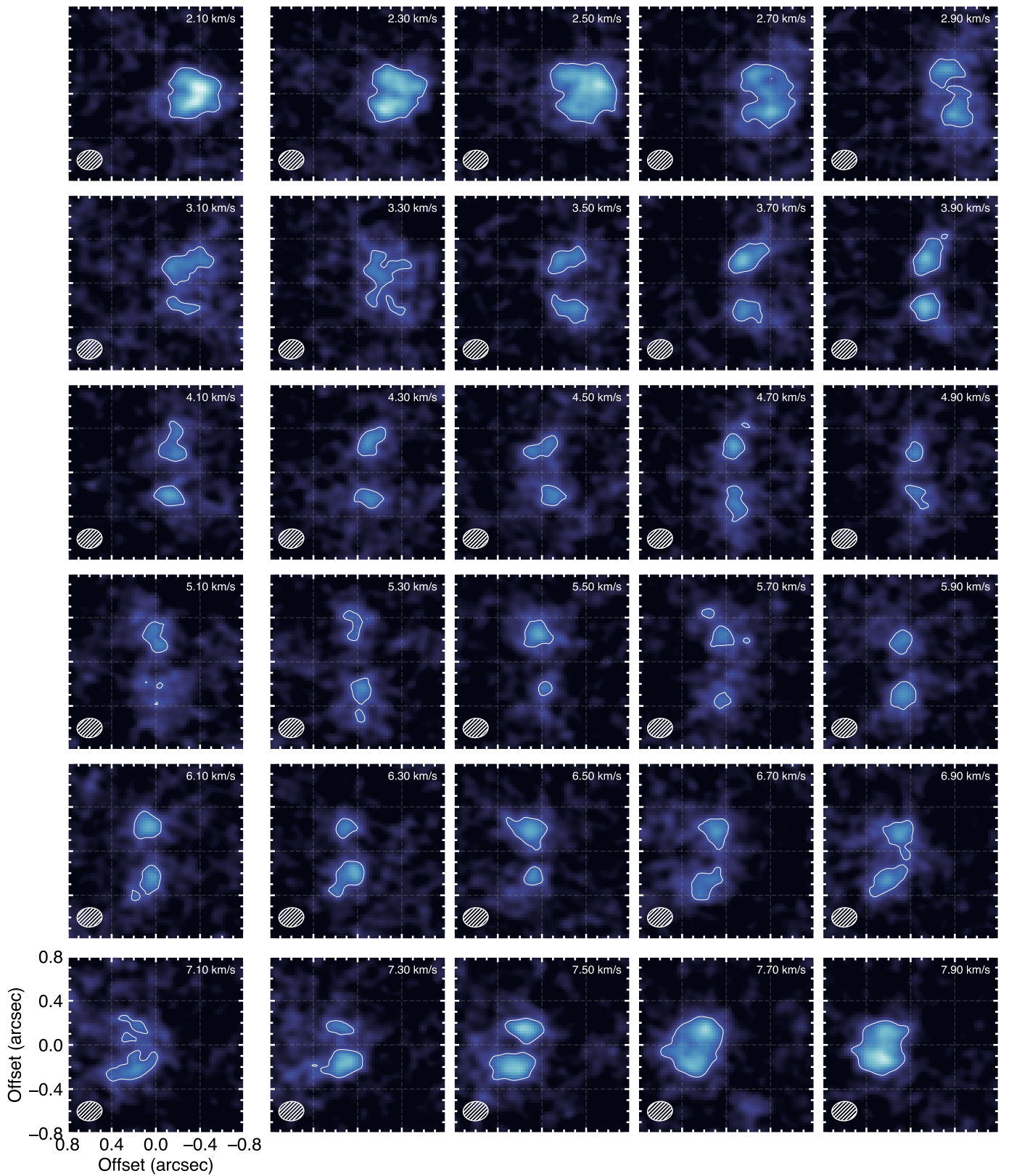


Fig. E.4: Same as Fig. E.2 but for the C^{18}O $J = 2 - 1$ molecular line with a beam of $0.22'' \times 0.17''$ and imaged at a channel spacing of 200 m s^{-1} .

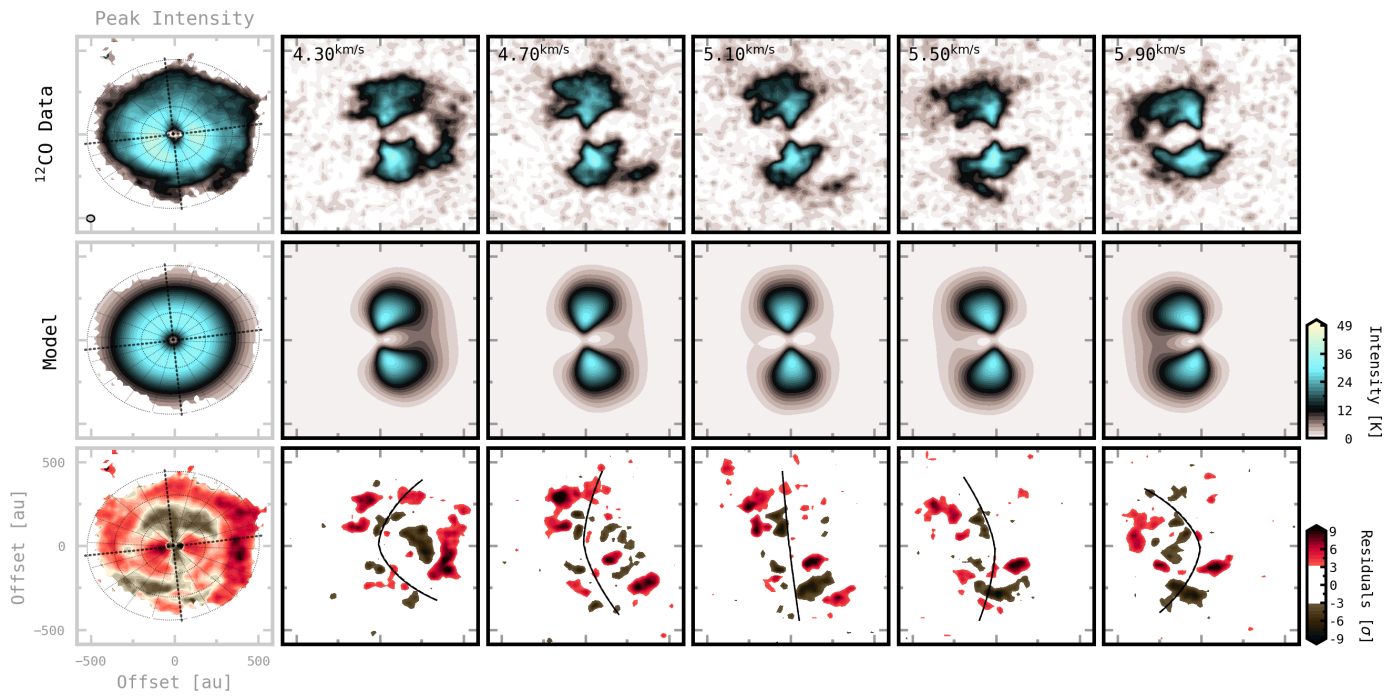


Fig. E.5: Selected line intensity channels for ^{12}CO $J = 2 - 1$ using the high-resolution cubes. The panels for each figure display the data channels, the best-fit model, and the residuals, from top to bottom. Residuals below $3\sigma = 5.0$ K are whited out. The systemic-velocity channel is at 5.1 km s^{-1} , and the left-most panels show the corresponding peak intensity maps.

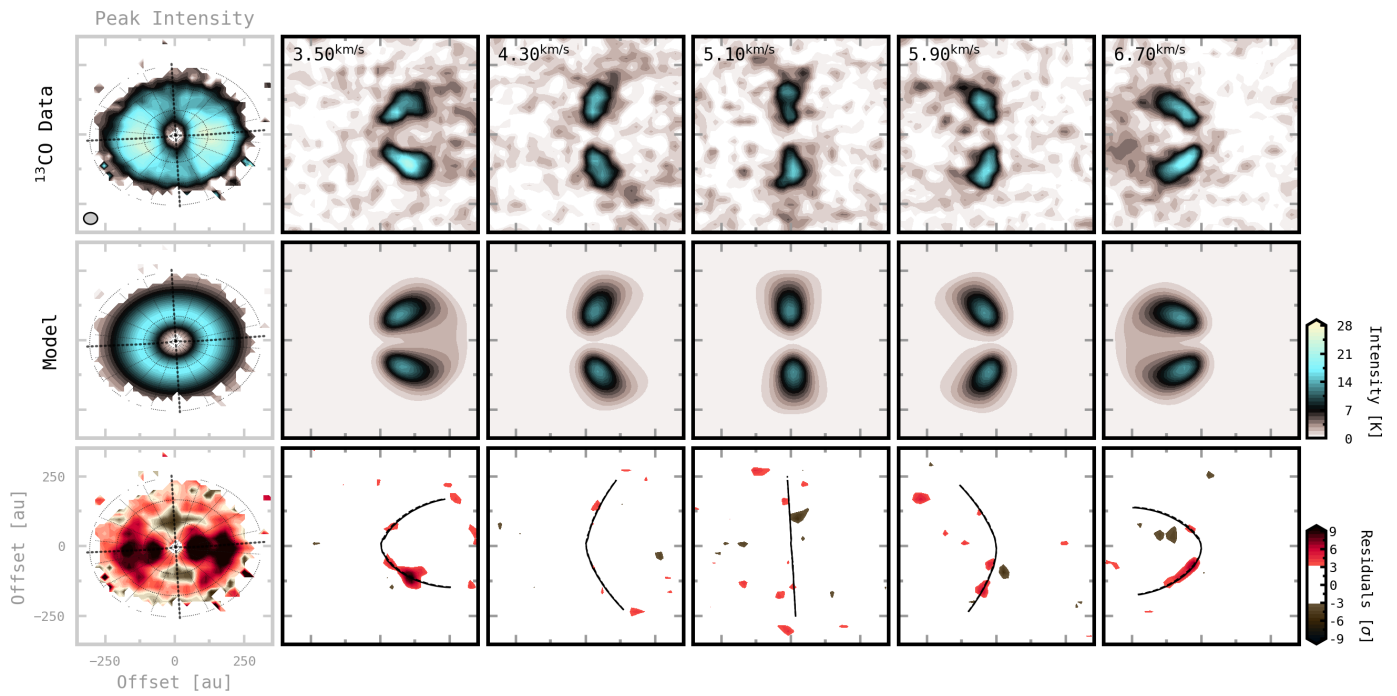


Fig. E.6: Same as Fig. E.5 but for ^{13}CO $J = 2 - 1$ using the high-resolution cube with residuals below $3\sigma = 3.6$ K are whited out.

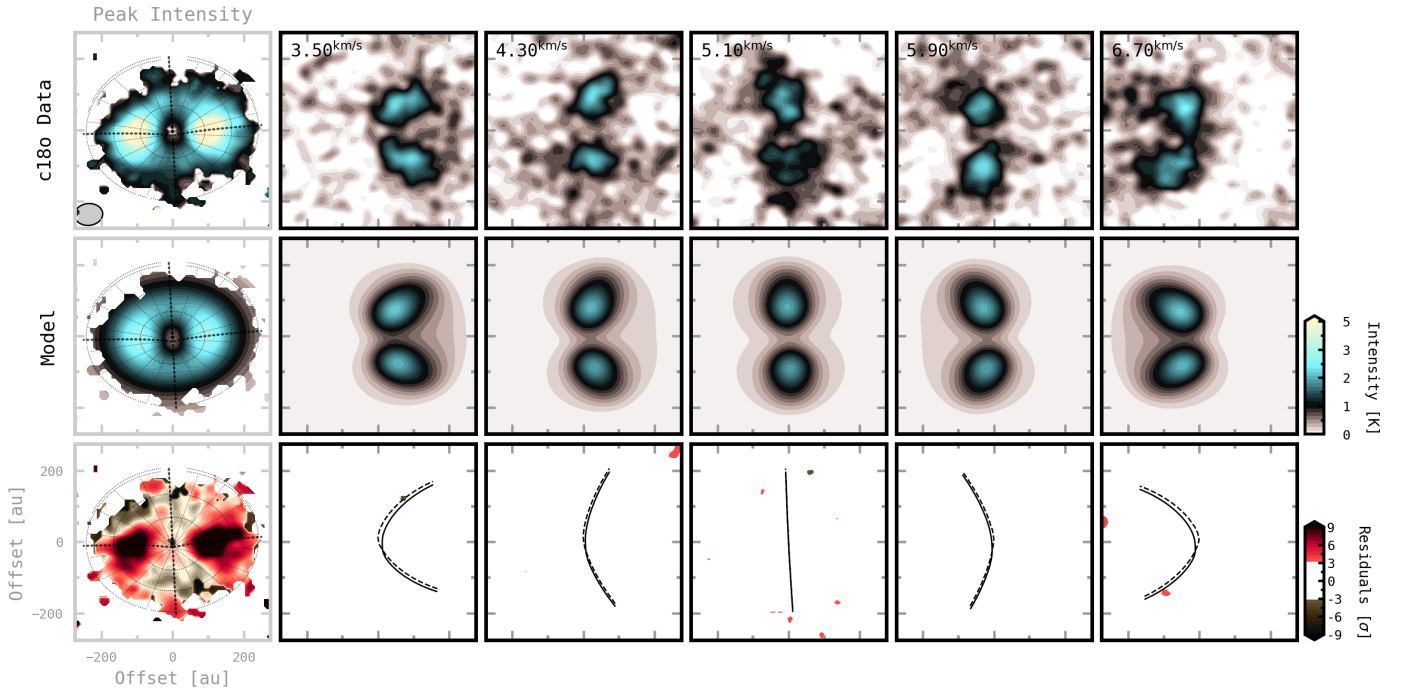


Fig. E.7: Same as Fig. E.5 but for C^{18}O $J = 2 - 1$ using the fiducial cube with residuals below $3\sigma = 3.0$ K are whited out. Note that there are nearly no residuals above 3σ due to the low S/N of the data.

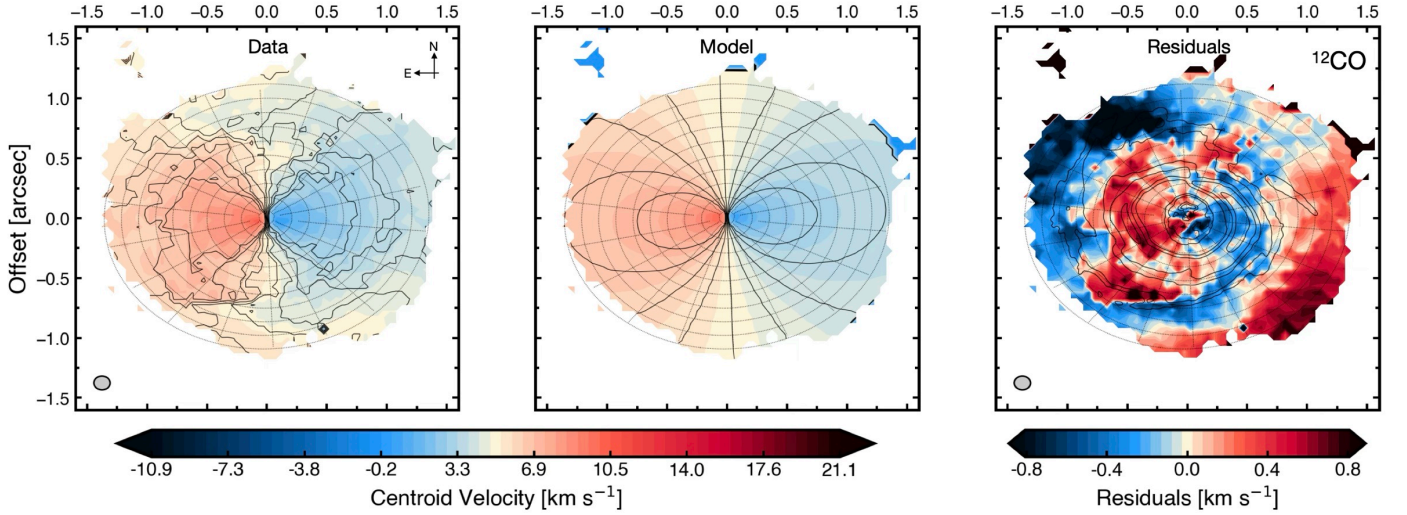


Fig. E.8: ^{12}CO quadratic velocity residuals. Here we use the bettermoments “quadratic” centroid moment, which fits a quadratic function to the peak of the line and its two neighboring pixel to determine the line centroid (Teague 2019b). The employed ^{12}CO robust 0.5 cube, Keplerian disciner model, and layout is the same as in Fig. 7. The quadratic LoS velocity map of the data differs from the Gaussian one of Fig. 7. The “quadratic” line centroid traces more closely the peak of the emission, hence leading to strong bending of the iso-velocity contours coinciding with the regions of broadened line-profiles, as highlighted in the map of Fig. 6. In particular, at the location of the infalling material in the southeast, this leads to a strong blue- or redshifted residual due to the double-peaked line profile at this location.

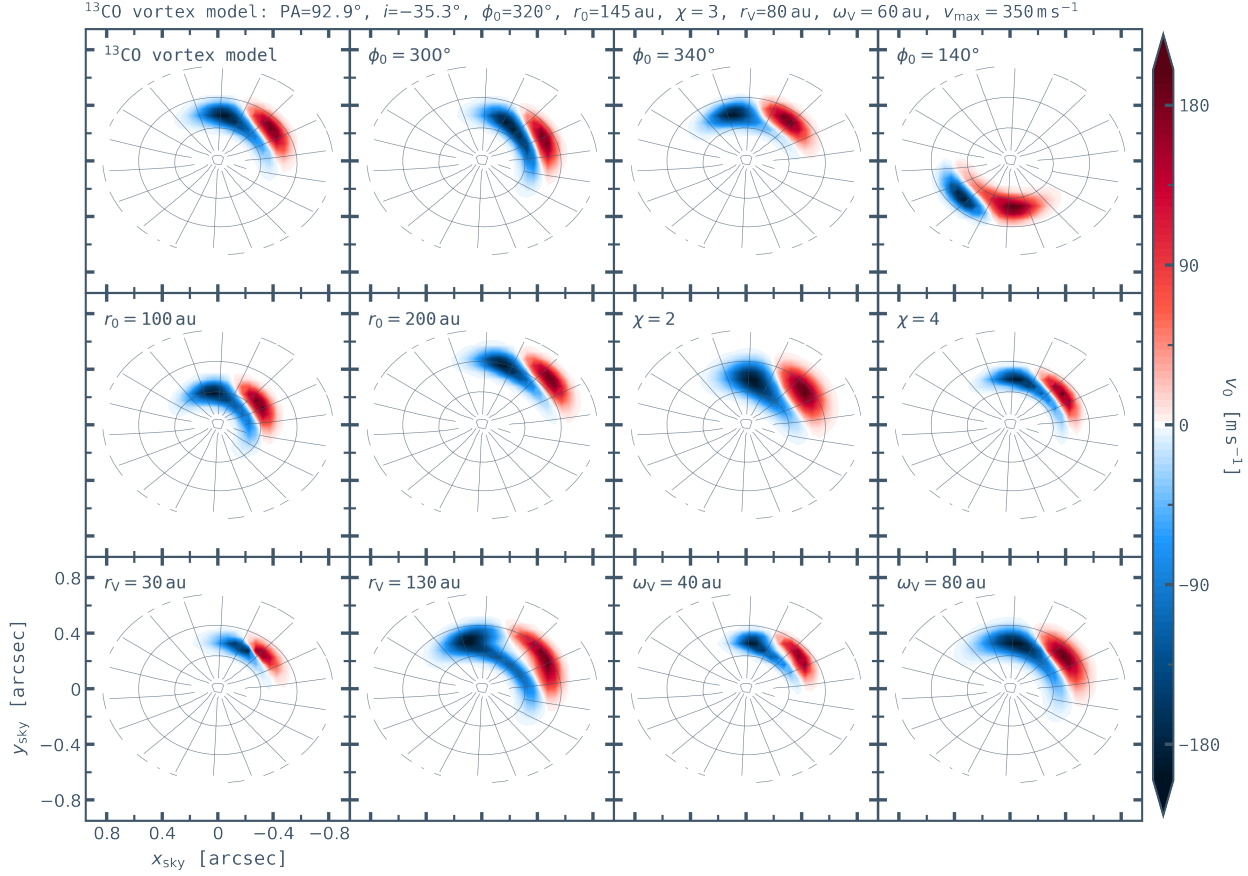


Fig. E.9: Line-of-sight velocities resulting from the analytical vortex model of Wölfer et al. (2025). The model best describing the ^{13}CO velocity residuals (Fig. 8) is shown in the upper left panel with employed parameters listed on the top of the figure. All the other panels vary one of these best-fit parameters to show how the resulting $v_{\text{l.o.s.}}$ changes. Position angle and inclination are taken from the ^{13}CO best-fit Keplerian model (Table C.1). Parameters ϕ_0 and r_0 are the angle and radial center of the continuum crescent. The remaining parameters describe the radius of the ring of maximum velocity (r_v), the Gaussian width of the vortex ring (ω_v), its aspect ratio (χ , for $\chi = 1$ the vortex is circular), and the maximum velocity of vortex rotation (v_{max} ; see Fig. 3 of Wölfer et al. 2025 for a sketch).